

A three-dimensional variational data assimilation scheme for the Regional Ocean Modeling System: Implementation and basic experiments

Zhijin Li,¹ Yi Chao,¹ James C. McWilliams,² and Kayo Ide²

Received 30 November 2006; revised 18 September 2007; accepted 19 December 2007; published 3 May 2008.

[1] A three-dimensional variational data assimilation scheme for the Regional Ocean Modeling System (ROMS), named ROMS3DVAR, has been described in the work of Li et al. (2008). In this paper, ROMS3DVAR is applied to the central California coastal region, an area characterized by inhomogeneity and anisotropy, as well as by dynamically unbalanced flows. A method for estimating the model error variances from limited observations is presented, and the construction of the inhomogeneous and anisotropic error correlations based on the Kronecker product is demonstrated. A set of single observation experiments illustrates the inhomogeneous and anisotropic error correlations and weak dynamic constraints used. Results are presented from the assimilation of data gathered during the Autonomous Ocean Sampling Network (AOSN) experiment during August 2003. The results show that ROMS3DVAR is capable of reproducing complex flows associated with upwelling and relaxation, as well as the rapid transitions between them. Some difficulties encountered during the experiment are also discussed.

Citation: Li, Z., Y. Chao, J. C. McWilliams, and K. Ide (2008), A three-dimensional variational data assimilation scheme for the Regional Ocean Modeling System: Implementation and basic experiments, *J. Geophys. Res.*, *113*, C05002, doi:10.1029/2006JC004042.

1. Introduction

[2] We recently developed a three-dimensional variational data assimilation scheme (3DVAR) for the Regional Ocean Modeling System and named the scheme ROMS3DVAR. The theoretical formulation of the scheme was presented by Li et al. [2008]. In this paper, we describe the implementation of the proposed scheme and illustrate the importance of the major formulations proposed by Li et al. [2008].

[3] The performance of 3DVAR hinges on the specification of the background error covariance matrices and the incorporation of dynamic constraints. In the work of Li et al. [2008], we proposed particular formulations for constructing the background error correlations and incorporating dynamic constraints. A Kronecker product method was proposed to construct background error correlations. This formulation allows us to construct three-dimensional (3-D) correlations, which enables us to incorporate some major aspects of inhomogeneity and anisotropy in coastal oceans, while rendering ROMS3DVAR computationally efficient and reliable. Concerning dynamic constraints, the weak geostrophic and hydrostatic formulations are used. Using these formulations, ROMS3DVAR demonstrated the capa-

bility to assimilate a variety of observations simultaneously, including satellite altimetry sea surface heights (SSHs), satellite sea surface temperatures (SSTs), temperature/salinity (*T/S*) profiles from various observational platforms, Acoustic Doppler Current Profiler (ADCP) current data, and high-frequency (HF) radar sea surface current data.

[4] For the purposes of illustration and evaluation, we apply the scheme to the central California coastal region. Although the ROMS3DVAR scheme is formulated as generally as possible and hence can be applied to any coastal region, there are several reasons for us to focus on central California in this study. It is one of the most sampled and investigated coastal regions [e.g., Hickey, 1998]; the unbalanced properties of the flow related to strong spring and summer upwelling [e.g., Hickey, 1998] make it dynamically very interesting; we have extensive experience modeling the central California coastal ocean [e.g., Marchesiello et al., 2003]; and the Coupled Ocean/Atmosphere Mesoscale Prediction System (COAMPS) [Hodur, 1997] provides us with continuous high-resolution atmospheric forcing [Chao et al., 2003; Y. Chao et al., Development, implementation and evaluation of a data-assimilative ocean forecasting system off the central California coast, submitted to Deep Sea Research, 2008]. Further, ROMS3DVAR was used in the Autonomous Ocean Sampling Network (AOSN) Monterey Field Experiment undertaken during August 2003 in the area surrounding Monterey Bay, California (for details, see <http://aosn.mbari.org>). This experiment demonstrated an unprecedented in situ observational capability for coastal oceans and collected large amounts of data from a variety of observational platforms, including satellites, airplanes, ships,

¹Jet Propulsion Laboratory, California Institute of Technology, Pasadena, California, USA.

²Department of Atmospheric and Oceanic Sciences and Institute of Geophysics and Planetary Physics, University of California, Los Angeles, California, USA.

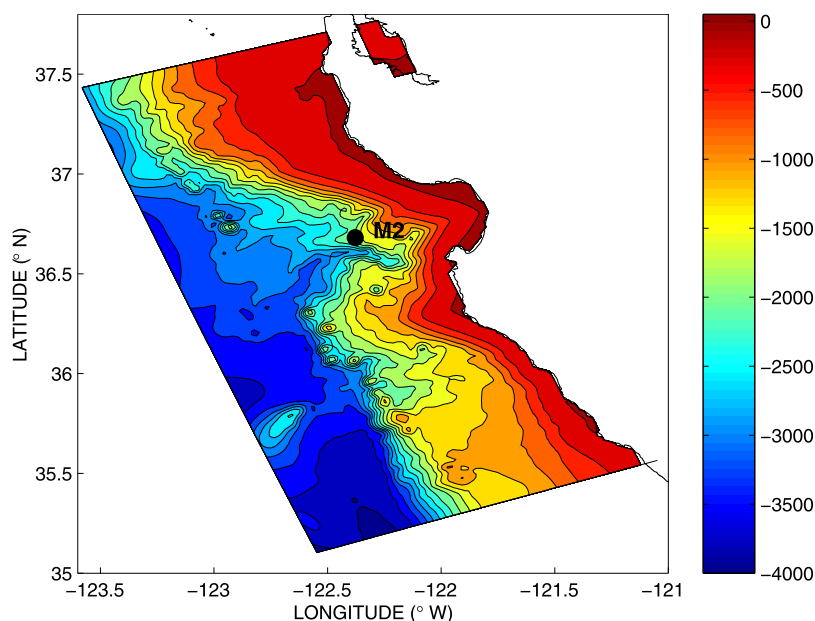


Figure 1. The bathymetry contour interval is 250 m. The black circle shows the location of the M2 mooring at 122.378°W and 36.697°N. The sharp trough near M2 is the Monterey Submarine Canyon.

drifters, buoys, autonomous underwater vehicles, and, in particular, a fleet of undersea gliders.

[5] For evaluation and validation, we focus on the following three aspects. First, the error covariances are examined in detail. A method for estimating error covariances with model generated data is described, and the features of the constructed error covariances are discussed to highlight their anisotropy, inhomogeneity and inseparability. Also, the importance of the weak dynamic constraints is examined. Second, we will present a set of single-observation influence experiments that exhibit the structures of the specified correlations, as suggested by Parrish and Derber [1992] and Thepaut et al. [1996]. The analysis increments from single-observation influence experiments are proportional to the covariances of the background errors, allowing us to examine how ROMS3DVAR responds to observations. Finally, the performance of ROMS3DVAR during August 2003 is evaluated against the AOSN data.

[6] The outline of this paper is as follows: In section 2, we briefly describe the basic configuration of ROMS and ROMS3DVAR as well as the atmospheric forcing. Section 3 describes the estimation of the background error covariance. In section 4 we present the single-observation influence experiments to examine the behavior of ROMS3DVAR. Section 5 presents experiments that assimilate observations from the AOSN experiment. Our focus here is on examining the performance of ROMS3DVAR and investigating some major issues of coastal data assimilation, such as the weak geostrophic constraint. Finally, section 6 discusses and summarizes the main results obtained in this study.

2. ROMS3DVAR Configuration for the U.S. West Coastal Ocean

2.1. ROMS Nested Configuration and Atmospheric Forcing

[7] ROMS is a free-surface, hydrostatic, three-dimensional primitive equation regional ocean model [Shchepetkin and

McWilliams, 2005, 2008; Marchesiello et al., 2001]. The vertical discretization uses a stretched terrain-following coordinate (S -coordinate) on a staggered grid over variable topography [Song and Haidvogel, 1994]. The stretched coordinate allows increased resolution in areas of interest, such as the thermocline and bottom boundary layers. The horizontal discretization uses a boundary-fitted, orthogonal curvilinear coordinate on a staggered Arakawa C-grid [Arakawa and Lamb, 1977]. Coastal boundaries are specified as a finite-discretized grid via land/sea masking. The lateral boundary condition is no-normal-flow at the coast.

[8] ROMS has a one-way nesting capability [Blayo and Debreu, 1999]. As described by Chao et al. (submitted manuscript, 2008), a three-level, nested configuration is used in this study: the largest domain (L0) covers the U.S. West Coastal Ocean at a horizontal resolution of 15km; the next (L1) is nested in L0 covering the central California coastal ocean at a horizontal resolution of 5 km; the last (L2) is nested in L1 and focuses on the region around Monterey Bay at a horizontal resolution of 1.5 km. The open ocean boundary condition for L2 is determined by L1, that of L1 by L0, and that of L0 by a climatological simulation of the Pacific ocean.

[9] All three nested levels have 32 layers in the vertical. Figure 1 shows the bathymetry and horizontal domain of L2, which is bounded by the California coast at the eastern edge and open ocean at the other three edges. A prominent feature of the bathymetry is the narrow shelf whose width varies along the coast. The slope is particularly steep along the Monterey Submarine Canyon. The numerical algorithms of ROMS are specifically designed to reduce pressure gradient errors associated with steep topography [Shchepetkin and McWilliams, 2003].

[10] In this study the atmospheric forcing is provided by hourly output from the Coupled Ocean and Atmosphere Mesoscale Prediction System (COAMPS), operated by the Naval Research Laboratory [Hodur, 1997]. COAMPS has a

quadruple nested-grid configuration with horizontal resolutions of 81, 27, 9, and 3 km for the largest to the smallest nested domain for the atmospheric model. The outputs from the 27 km, 9 km, and 3 km resolution COAMPS are used to force the L0, L1, and L2 domains of ROMS, respectively. The surface latent and sensible heat fluxes, as well as surface evaporation rates, are derived from sea surface air temperatures, sea surface relative humidities, 10 m winds and sea surface temperatures (SSTs) from the ocean model, using the bulk formulae proposed by *Kondo* [1975]. The fresh water flux is computed as the calculated evaporation rate minus the COAMPS precipitation rate (E-P). The wind stress is derived from the 10 m winds using the formula of *Large and Pond* [1982]. The COAMPS winds show good agreement with the observed winds from the Monterey Bay Aquarium Research Institute (MBARI) M2 mooring (Figure 2).

2.2. ROMS3DVAR Configuration

2.2.1. Incremental 3DVAR Scheme

[11] ROMS3DVAR is an incremental 3DVAR scheme, and it incorporates weak constraints based on hydrostatic balance and geostrophic balance. As such, ROMS3DVAR defines the cost function as follows:

$$J_c(\delta \mathbf{FF}x_c) = J_{\zeta'}^b(\delta \mathbf{FF}x_{\zeta'}) + J_{\psi''\chi''}^b(\delta \mathbf{FF}x_{\psi''\chi''}) + J_{TS}^b(\delta \mathbf{FF}x_{TS}) + J_{\zeta'}^o(\delta \mathbf{FF}x_{\zeta'}, \delta \mathbf{FF}x_{TS}) + J_{uv}^o(\delta \mathbf{FF}x_{\zeta'}, \delta \mathbf{FF}x_{\psi''\chi''}, \delta \mathbf{FF}x_{TS}) + J_{TS}^o(\delta \mathbf{FF}x_{TS}). \quad (1)$$

[12] In the cost function, there are five different control variables, $\delta \mathbf{FF}x_{\zeta'}$, $\delta \mathbf{FF}x_{\psi''}$, $\delta \mathbf{FF}x_{\chi''}$, $\delta \mathbf{FF}x_{TS}$ and $\delta \mathbf{FF}x_S$. Following the notation introduced by *Li et al.* [2008], $\mathbf{FF}x$ and $\delta \mathbf{FF}x$ are the model state and its increment on the ROMS3DVAR grid (defined in section 2.2.2), respectively; the subscripts ζ' , ψ'' , χ'' , T , and S correspond to the nonsteric SSH, ageostrophic streamfunction, ageostrophic velocity potential, temperature, and salinity. All control variables are 3-D, except the nonsteric 2-D SSH. The background cost function consists of

$$J_{\zeta'}^b = \frac{1}{2} \delta \mathbf{FF}x_{\zeta'}^T \mathbf{FF}b_{\zeta'}^{-1} \delta \mathbf{FF}x_{\zeta'} \\ J_{\psi''\chi''}^b = \frac{1}{2} \delta \mathbf{FF}x_{\psi''\chi''}^T \mathbf{FF}b_{\psi''\chi''}^{-1} \delta \mathbf{FF}x_{\psi''\chi''} \\ J_{TS}^b = \frac{1}{2} \delta \mathbf{FF}x_{TS}^T \mathbf{FF}b_{TS}^{-1} \delta \mathbf{FF}x_{TS}, \quad (2)$$

where $\mathbf{FF}b_{\zeta'}$, $\mathbf{FF}b_{\psi''\chi''}$, and $\mathbf{FF}b_{TS}$ are the background error covariances corresponding to nonsteric SSH, ageostrophic streamfunction and velocity potential, and T and S . The observational cost function consists of

$$J_{\zeta'}^o = \frac{1}{2} (\mathbf{\Pi} \delta \mathbf{FF}x_{TS} + \delta \mathbf{FF}x_{\zeta'} - \mathbf{FF}d_{\zeta'})^T \mathbf{FF}r_{\zeta'}^{-1} \cdot (\mathbf{\Pi} \delta \mathbf{FF}x_{TS} + \delta \mathbf{FF}x_{\zeta'} - \mathbf{FF}d_{\zeta'}) \\ J_{uv}^o = \frac{1}{2} (\mathbf{\Gamma}_{\zeta'} \delta \mathbf{FF}x_{\zeta'} + \mathbf{\Gamma}_{TS} \delta \mathbf{FF}x_{TS} + \mathbf{\Phi} \delta \mathbf{FF}x_{\psi''\chi''} - \mathbf{FF}d_{uv})^T \cdot \mathbf{FF}r_{uv}^{-1} (\mathbf{\Gamma}_{\zeta'} \delta \mathbf{FF}x_{\zeta'} + \mathbf{\Gamma}_{TS} \delta \mathbf{FF}x_{TS} + \mathbf{\Phi} \delta \mathbf{FF}x_{\psi''\chi''} - \mathbf{FF}d_{uv}) \\ J_{TS}^o = \frac{1}{2} (\delta \mathbf{FF}x_{TS} - \mathbf{FF}d_{TS})^T \mathbf{FF}r_{TS}^{-1} (\delta \mathbf{FF}x_{TS} - \mathbf{FF}d_{TS}), \quad (3)$$

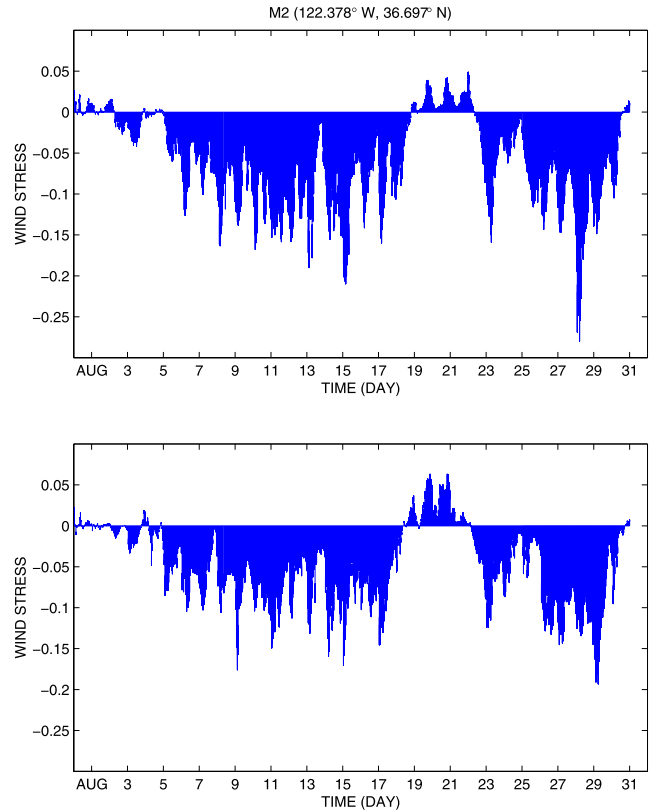


Figure 2. Hourly alongshore wind stress derived from 10 m winds at M2 for August 2003: (top) observation and (bottom) COAMPS. The unit is N/m^2 . For the location of M2, see Figure 1.

where $\mathbf{FF}d_{\zeta'}$, $\mathbf{FF}d_{uv}$ and $\mathbf{FF}d_{TS}$ are the innovation vectors of SSH, the velocity components and T/S , and $\mathbf{FF}r_{\zeta'}$, $\mathbf{FF}r_{uv}$, and $\mathbf{FF}r_{TS}$ are the corresponding observational error covariances. The matrix operator $\mathbf{\Phi}$ is used for computing steric SSH increments, $\mathbf{\Gamma}$ for computing geostrophic velocity increments, and $\mathbf{\Phi}$ for computing velocity components from streamfunction and velocity potential.

2.2.2. ROMS3DVAR Implementation

[13] ROMS3DVAR executes data assimilation for each nested level. Because all levels use the same formulation, we focus in the subsequent discussions on L2, which has the smallest domain but the highest horizontal resolution. For consistency with the ROMS open boundary conditions, ROMS3DVAR takes the forecast and returns the analysis at all ROMS L2 model grid points but not at those determined by L1.

[14] To handle the large-dimension background error covariance matrices while taking anisotropy and inhomogeneity into account, ROMS3DVAR computes a three-dimensional (3-D) correlation matrix as a Kronecker product $\mathbf{FF}c^{\xi\kappa} \otimes \mathbf{FF}c^{\eta}$ of a two-dimensional (2D) matrix $\mathbf{FF}c^{\xi\kappa}$ in the vertical and cross-shore directions and a one-dimensional (1-D) matrix $\mathbf{FF}c^{\eta}$ in the alongshore direction [*Li et al.*, 2008]. Here ξ , η and κ stand for the alongshore, cross-shore and vertical directions, respectively. ROMS3DVAR also

computes the 2-D surface correlation matrix $\mathbf{FFc}^{\xi\eta}$ for nonsteric SSH as a Kronecker product, that is, $\mathbf{FFc}^{\xi} \otimes \mathbf{FFc}^{\eta}$.

[15] Any $\mathbf{FFc}^{\xi\kappa}$, \mathbf{FFc}^{ξ} or \mathbf{FFc}^{η} is grid-based, i.e., correlations are defined between two grid points. A difficulty arises, however, in constructing $\mathbf{FFc}^{\xi\kappa}$ using the S -coordinate in the presence of variable topography. To illustrate this, let us consider an error correlation $C^{\xi\kappa}(i_1 k_1, i_2 k_1)$ between a nearshore grid point $(i_1 k_1)$ and a grid point $(i_2 k_1)$ 15 km offshore and on the same S -level k_1 near the ocean bottom in two different vertical cross-shore sections. In a section south of Monterey Bay, the depth at $(i_1 k_1)$ is about 10 m and at $(i_2 k_1)$ about 500 m (Figure 1). Because the depth of thermocline and mixed layer in this region is about 30 m in late summer and less than 100 m in winter, $C^{\xi\kappa}(i_1 k_1, i_2 k_1)$ between these two 2-D grid points should be near zero. In a section north of the bay, however, $C^{\xi\kappa}(i_1 k_1, i_2 k_1)$ may not necessarily be zero because the depth of the grid point $(i_2 k_1)$ is much shallower than 500m. This variation in the correlations presents a fundamental difficulty in constructing $\mathbf{FFc}^{\xi\kappa}$ using the S -coordinate.

[16] To circumvent the difficulty, the ROMS3DVAR grid employs a Z -coordinate for the vertical discretization. The same staggered ROMS C-grid is used in the horizontal so that the resulting analysis will easily satisfy the lateral boundary condition. In this study the ROMS3DVAR grid uses $N^{\xi} \times N^{\eta} = 82 \times 178$ horizontal curvilinear grid points, and $N^{\kappa} = 24$ vertical Z -levels in L2.

[17] Accordingly, the execution of the incremental 3DVAR given a ROMS forecast on the S -coordinate is accomplished through the following procedure. Using spline interpolation [Akima, 1970], the background state on the Z -coordinate is first formed by transforming the ROMS forecast. After performing the incremental 3DVAR, the lateral boundary condition along the coastline is imposed on the analysis increment in the Z -coordinate. ROMS3DVAR produces the final analysis by transforming and adding the analysis increment to the original ROMS forecast on the S -coordinate. The transformation back to the S -coordinate is performed on the analysis increment (not the full analysis) to reduce the interpolation errors and thus help maintain the delicate dynamical balance that is attained by forward model integration in the ROMS forecast. A concern may arise, however, concerning whether the final analysis satisfies the lateral boundary condition on the S -coordinate. To address this concern, we examined the final analysis in various experiments and found that the lateral boundary condition is, in general, adequately satisfied.

[18] For the estimation of coastal ocean dynamics with timescales ranging from hours to days, we adopted for ROMS3DVAR a 6-h assimilation cycle. The first cycle of the day begins by performing a 6-h ROMS forecast using the analysis valid at 0300 UTC as an initial condition; 0300 UTC corresponds to 7 pm local standard time (LST). Once the valid 0900 UTC 6-h ROMS forecast is completed and all observations in the 6-h time bin between 0600 and 1200 UTC are collected, ROMS3DVAR executes the incremental 3DVAR and computes the analysis valid at 0900 UTC by treating all observations as if they were taken at 0900 UTC. This completes the first 6-h cycle. ROMS3D-

VAR repeats the cycle four times a day and produces analyses valid at 0300, 0900, 1500, and 2100 UTC.

3. Estimation of Standard Deviation and Correlation Matrices

[19] Having described the general ROMS-DAS procedure and its grid arrangement, we turn our attention to the issues concerning estimation of the standard deviation matrices and the correlation matrices for the background errors. This section presents a general method for estimation of the standard deviation and correlation matrices associated with \mathbf{FFb}_{ζ} , $\mathbf{FFb}_{\psi/\chi}$, and \mathbf{FFb}_{TS} , along with its application to ROMS3DVAR.

3.1. Generation of the Surrogate Data Set

[20] Estimation of the 3DVAR standard deviation and correlation matrices requires a large data set that represents the forecast-error statistics of the data assimilation system. Two methods have been suggested for constructing such a data set. One method uses observations as a sampling of the true state [Hollingsworth and Lonnberg, 1986; Phillips, 1986]. The other method uses the difference between two forecasts valid at the same time but with distinct lead times as a representation of the forecast error [Parrish and Derber, 1992]. This is the so-called NMC method, where NMC stands for the National Meteorological Center (now the National Center for Environmental Prediction). An advantage of the NMC method is the proficient generation of a large data set for any control variable. While Parrish and Derber [1992] cautiously described it as a crude first step, the NMC method has been used operationally at major meteorological centers [e.g., Rabier et al., 1998; Barker et al., 2004]. The usefulness of the data sets generated by the NMC method depend implicitly on the quality and number of observations used in the data assimilation system.

[21] Although the California coastal ocean is one of the most sampled coastal oceans, almost all observations are still sporadic, sampled monthly or even seasonally at irregular locations. An example is the California Cooperative Ocean Fisheries Investigation (CalCOFI) (<http://calcofi.org>), which provides only seasonal sampling. For ROMS3DVAR, which uses a high-resolution model to forecast coastal ocean dynamics with time scales ranging from hours to days, such observations are simply inadequate for use in either of the two above-mentioned methods of building large, reliable data sets.

[22] We therefore employ an alternate method. With an ensemble of long-time ROMS simulations, our method assembles a surrogate data set where the standard deviation matrices and the correlation matrices are estimated using a limited number of observations. The ensemble is designed to account for forecast errors due to atmospheric forcing, model errors, and initial conditions. For errors in atmospheric forcing, we use two types of atmospheric forcing derived from the hourly COAMPS output for the period from 20 July 2003 to 31 October 2004: 3 h means and daily means. For model errors, we use two vertical resolutions in ROMS: 20 levels and 32 levels. For errors in the initial condition, we use six different initial conditions in the four ensembles (see Table 1). These six initial conditions are randomly selected from six independent ROMS simulations.

Table 1. Allocation of Six Ensemble Members to Four Settings Based on Two Types of Atmospheric Forcing and Two Levels of Vertical Resolution

		Model	
		20 Levels	32 Levels
Atmospheric forcing	3 h	2	2
	daily	1	1

To assemble a surrogate data set that contains time scales ranging from hours to days, we sample at 0300, 0900, 1500, and 2100 UTC daily, the same times as the ROMS analysis, from 1 November 2003 to 31 October 2004. The two time levels at 0300 and 1500 UTC correspond to 7 pm and 7 am LST and represent the diurnal variation.

[23] With the ROMS ensemble simulations in hand, a surrogate data set is built using the following procedure. First, we compute the 12 monthly means and form a perturbation data set by removing the corresponding monthly means. Then the monthly means and the perturbation data set are interpolated to the ROMS3DVAR grid on the Z-coordinate (section 2). Next, the perturbation data set is transformed to the ROMS3DVAR control variables: nonsteric SSH is obtained from temperature, salinity, and SSH based on the hydrostatic relation [Li *et al.*, 2008, equation (14)]. The geostrophic streamfunction and velocity potential are derived from the nonsteric SSH, temperature, salinity, and horizontal velocity based on the geostrophic relation [Li *et al.*, 2008, equation (17)]. The hydrostatic and geostrophic operators used in these transformations are computed using the corresponding monthly means [Li *et al.*, 2006, 2008, Appendix A]. Finally, we remove the ensemble monthly mean of the perturbation to enforce the mean-zero condition on the perturbation of the ROMS3DVAR control variables.

[24] Owing to the seasonal transition of upwelling in the region, the thermocline shows a significant seasonal variability, which leads to a seasonal variability of correlations, particularly vertical correlations. As such, ROMS3DVAR uses monthly standard deviation matrices and correlation matrices. Each monthly matrix is derived using 3 months of data including the previous and subsequent months. In this way, transitions from one month to the next are relatively smooth. For the rest of this paper, we discuss August only because our experiments in the following sections use observations taken in August 2003 during the AOSN experiment (see section 5).

[25] For simplicity in presentation, we formulate the standard deviation and correlation matrices for the case where the ocean domain is a 3-D box with a flat bottom, but the actual ROMS3DVAR uses an extension of the formulae to an irregular domain. The five control variables that make up the surrogate data are $\Delta x_{\zeta}^{\xi\eta}$, $\Delta x_{\psi}^{\xi\eta\kappa}$, $\Delta x_{\chi}^{\xi\eta\kappa}$, $\Delta x_T^{\xi\eta\kappa}$, and $\Delta x_S^{\xi\eta\kappa}$. We index a control variable by $\{\Delta x^{\xi\eta\kappa}(ijk, t, m)\}$: $i \in [1, N^{\xi}]$, $j \in [1, N^{\eta}]$, and $k \in [1, N^{\kappa}]$ for the 3D space; $t \in [1, N_t]$ for time with $N_t = 4 \times 92$; and $m \in [1, M_{en}]$ for the ensemble member with $M_{en} = 6$. All formulae also apply to 2-D variables $\Delta x_{\zeta}^{\xi\eta}$, simply suppress the vertical direction, that is, $N^{\kappa} = 1$.

3.2. Standard Deviation Matrices

[26] We first present a method for estimating a 3-D standard deviation matrix $\Sigma^{\xi\eta\kappa}$ from the surrogate data $\{\Delta x^{\xi\eta\kappa}(ijk, t, m)\}$: $\Sigma^{\xi\eta\kappa}$ represents any of $\Sigma_{\zeta}^{\xi\eta}$, $\Sigma_{\psi}^{\xi\eta\kappa}$, $\Sigma_{\chi}^{\xi\eta\kappa}$, $\Sigma_T^{\xi\eta\kappa}$, or $\Sigma_S^{\xi\eta\kappa}$ the five control variables.

3.2.1. Formulation

[27] There are two reasons why the standard deviations computed from the surrogate data cannot be used directly as the standard deviations of the forecast errors. One is that the statistics of the surrogate data do not necessarily represent those of the forecast errors. As we continue to assimilate, the actual forecast errors should become smaller and the deviation from the surrogate data statistics increases. The forecast errors also depend on the spatial distribution of observations over time. A third reason is the presence of small spatial scales in the standard deviation computed from the surrogate data at each grid point (Figure 3). These small spatial scales may be caused by the topographic variations or noise due to a finite sampling of the surrogate data. Either way, the presence of small spatial scales in the standard deviation introduces undesirable small spatial scales in the analysis increment.

[28] To construct $\Sigma^{\xi\eta\kappa}$, we first compute the “structure function” $\hat{\sigma}^{\xi\kappa}(ik)$, which is an alongshore average of the standard deviation of the surrogate data:

$$(\hat{\sigma}^{\xi\kappa}(ik))^2 = \frac{1}{N^{\eta}M_tM_{en}} \sum_{j=1}^{N^{\eta}} \sum_{t=1}^{M_t} \sum_{m=1}^{M_{en}} (\Delta x^{\xi\eta\kappa}(ijk, t, m) - \bar{\Delta x}^{\xi\kappa}(ik))^2, \quad (4)$$

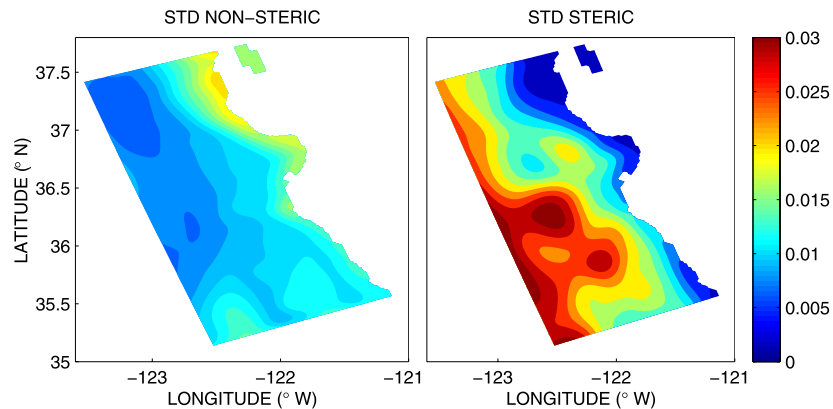


Figure 3. Standard deviation of the (left) nonsteric SSH and (right) steric SSH computed from the surrogate data at each grid point. The unit is meters.

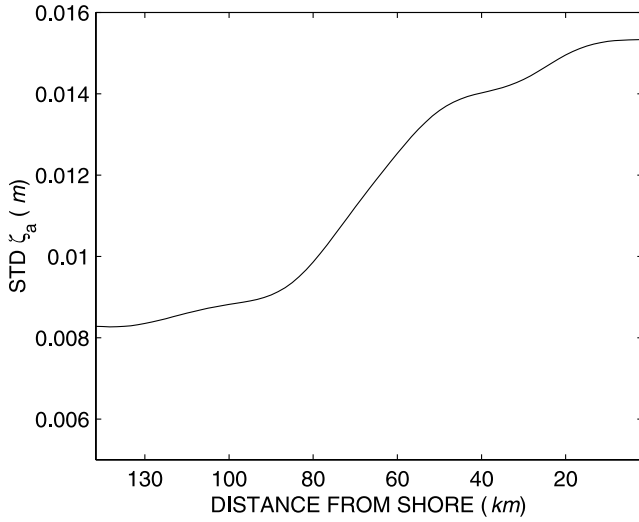


Figure 4. The structure function $\hat{\sigma}_{\zeta}^{\xi}(i)$ of the nonsteric SSH as a function of cross-shore distance from the coast, corresponding to the left panel of Figure 3.

where

$$\Delta \bar{x}^{\xi\kappa}(ik) = \frac{1}{N^{\eta} M_t M_{en}} \sum_{j=1}^{N^{\eta}} \sum_{t=1}^{M_t} \sum_{m=1}^{M_{en}} \Delta x^{\xi\eta\kappa}(ijk, t, m). \quad (5)$$

We choose the alongshore average because there are relatively few alongshore variations in the standard deviation of the surrogate data (e.g., Figure 3). This is also consistent with the separability assumption of alongshore correlations from vertical cross-shore correlations used in the construction of correlation matrices (Li *et al.* [2006]; see also section 3.3 here). Figure 4 shows the structure function $\hat{\sigma}_{\zeta}^{\xi}(i)$ of the 2-D nonsteric SSH, obtained by suppressing the vertical direction in (4) and (5). The properties of the nonsteric SSH structure function are discussed further in section 3.2.2.

[29] The standard deviation matrix $\Sigma^{\xi\eta\kappa}$ is obtained by applying a tuning (scaling) parameter α . A diagonal entry of $\Sigma^{\xi\eta\kappa}$ corresponding to a grid point (ijk) is given by $\alpha \hat{\sigma}^{\xi\kappa}(ik)$. The tuning parameter α is sought to represent the ratio of actual forecast errors to those of the surrogate data.

In practice, α can be estimated using empirical rules or comparisons between forecasts and observations. When the number of observations is limited, a single value of α should be used to define $\Sigma^{\xi\eta\kappa}$ uniformly over all grid points. As more observations become available, α can become dependent on location to better represent the generally complex distribution of forecast errors.

3.2.2. Application

[30] Due to the limited number of observations, ROMS3DVAR currently uses a single α_{ζ} for $\Sigma_{\zeta}^{\xi\eta}$, a single $\alpha_{\psi''\chi''}$ for both $\Sigma_{\psi''}^{\xi\eta\kappa}$ and $\Sigma_{\chi''}^{\xi\eta\kappa}$, and a single α_{TS} for both $\Sigma_T^{\xi\eta\kappa}$ and $\Sigma_S^{\xi\eta\kappa}$.

[31] The structure function $\hat{\sigma}_{\zeta}^{\xi}(i)$ for the nonsteric SSH is shown in Figure 4. Far offshore, the steric SSH is dominant, which is consistent with large-scale model results [e.g., Fukumori *et al.*, 1998]. The amplitude of the nonsteric SSH decreases as the cross-shore distance from the coast increases. This implies that nearshore SSH changes are due to the water mass convergence and offshore changes due to the T/S changes. We choose $\alpha_{\zeta} = 0.5$ for $\Sigma_{\zeta}^{\xi\eta}$ based on a comparison of the ROMS3DVAR forecasts with altimetry observations.

[32] Figure 5 shows the structure functions $\hat{\sigma}_{\psi''}^{\xi\kappa}(ik)$ and $\hat{\sigma}_{\chi''}^{\xi\kappa}(ik)$ of ageostrophic streamfunction and ageostrophic velocity potential. Note that the streamfunction and velocity potential are not directly observed, but the velocity components are. To determine the scaling parameter $\alpha_{\psi''\chi''}$, we then use an empirical formula for the horizontal velocity suggested by Daley [1991, chap. 5.2]:

$$\frac{1}{2} (E_v^2 + E_u^2) = \alpha_{\psi''\chi''} \left(L_{g\psi}^{-2} \hat{\Sigma}_{g\psi}^2 + L_{\psi''}^{-2} \hat{\Sigma}_{\psi''}^2 + L_{\chi''}^{-2} \hat{\Sigma}_{\chi''}^2 \right). \quad (6)$$

The left-hand side represents the variance of differences between the model forecasts and observations in both velocity components. The right-hand side represents the variance of the velocity components computed from the streamfunction and velocity potential of the surrogate data set under the following assumptions: no correlation between ageostrophic streamfunction and ageostrophic velocity potential; no correlation between the errors of the geostrophic velocity and ageostrophic velocity; and isotropy of the ageostrophic streamfunction and the ageostrophic velocity potential. $L_{g\psi}$, $L_{\psi''}$ and $L_{\chi''}$ are decorrelation length

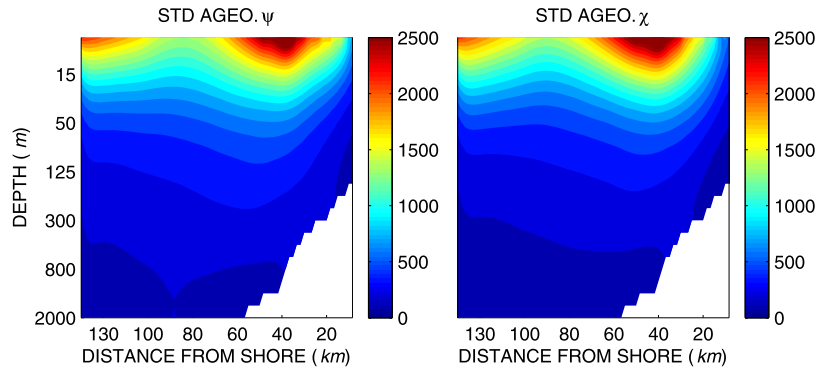


Figure 5. The structure functions $\hat{\sigma}_{\psi''}^{\xi\kappa}(ik)$ and $\hat{\sigma}_{\chi''}^{\xi\kappa}(ik)$ of (left) ageostrophic streamfunction and (right) ageostrophic velocity potential. The unit is s^{-1} . The white areas are the locations where there is no single grid point in the water along the entire shore.

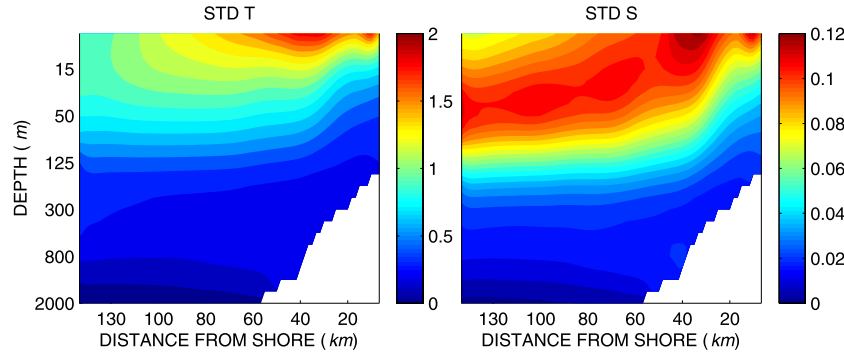


Figure 6. The structure functions of (left) temperature $\hat{\sigma}_T^{\xi\kappa}(ik)$ and (right) salinity $\hat{\sigma}_S^{\xi\kappa}(ik)$. The units are $^{\circ}\text{C}$ for temperature and psu for salinity.

scales for the standard deviations $\hat{\Sigma}_{\psi}$, $\hat{\Sigma}_{\psi''}$, and $\hat{\Sigma}_{\chi''}$, respectively. Based on the ROMS3DVAR forecasts and the Acoustic Doppler Current Profile (ADCP) measurements at the M2 mooring (Figure 1), we choose $\alpha_{\psi''\chi''} = 0.38$ for $\Sigma_{\psi''}^{\xi\eta\kappa}$ and $\Sigma_{\chi''}^{\xi\eta\kappa}$.

[33] Figure 6 shows the structure functions $\hat{\sigma}_T^{\xi\kappa}(ik)$ and $\hat{\sigma}_S^{\xi\kappa}(ik)$ for temperature and salinity in a vertical cross-shore section. The relatively large values of $\hat{\sigma}_T^{\xi\kappa}(ik)$ near the surface are due to variability forced by the atmosphere. In contrast, the relatively large values of $\hat{\sigma}_S^{\xi\kappa}(ik)$ are associated with thermocline variability. On the basis of a comparison of the ROMS3DVAR forecasts and available mooring observations, we choose $\alpha_{TS} = 0.35$ for $\Sigma_T^{\xi\eta\kappa}$ and $\Sigma_S^{\xi\eta\kappa}$.

3.3. Correlation Matrices

[34] Having constructed $\Sigma^{\xi\eta\kappa}$, we now present a method for estimating the self-correlation $\mathbf{FFc}^{\xi\eta\kappa}$ from the surrogate data: $\mathbf{FFc}^{\xi\eta\kappa}$ represents any of $\mathbf{FFc}_{\zeta\zeta'}^{\xi\eta}$, $\mathbf{FFc}_{\psi\psi''}^{\xi\eta\kappa}$, $\mathbf{FFc}_{\chi\chi''}^{\xi\eta\kappa}$, $\mathbf{FFc}_{TT}^{\xi\eta\kappa}$, or $\mathbf{FFc}_{SS}^{\xi\eta\kappa}$, though the vertical correlation are suppressed for the 2-D correlation matrix $\mathbf{FFc}_{\zeta\zeta'}^{\xi\eta}$. Because ROMS3DVAR uses a Kronecker product-based algorithm $\mathbf{FFc}^{\xi\eta\kappa} = \mathbf{FFc}^{\xi\kappa} \otimes \mathbf{FFc}^{\eta}$ to construct the self-correlation matrix [Li *et al.*, 2008], we describe a method for computing $\mathbf{FFc}^{\xi\kappa}$ and \mathbf{FFc}^{η} . We also present a method for estimating the error cross-correlation matrix $\mathbf{FFc}_{TS}^{\xi\eta\kappa}$ between temperature and salinity. Although the current ROMS3DVAR neglects the error cross-correlation between ageostrophic streamfunction and velocity potential, it can be incorporated by considering the cross-correlation $\mathbf{FFc}_{\psi\psi''}^{\xi\eta\kappa}$.

3.3.1. Formulation

[35] To compute the ROMS3DVAR self-correlation matrices, we assume that the correlations from the surrogate data have the same structure as the forecast errors. This allows us to compute $\mathbf{FFc}^{\xi\kappa}$ and \mathbf{FFc}^{η} for the five self-correlations directly from the surrogate data.

[36] An entry of $\mathbf{FFc}^{\xi\kappa}$, corresponding to the correlation between two 2-D grid points $(i_1 k_1)$ and $(i_2 k_2)$ in the vertical cross-shore section, is

$$C^{\xi\kappa}(i_1 k_1, i_2 k_2) = \frac{1}{\hat{\sigma}^{\xi\kappa}(i_1 k_1) \hat{\sigma}^{\xi\kappa}(i_2 k_2)} \cdot \frac{1}{N^{\eta} M_t M_{en}} \sum_{j=1}^{N^{\eta}} \sum_{t=1}^{M_t} \sum_{m=1}^{M_{en}} \cdot (\Delta x^{\xi\eta\kappa}(i_1 j k_1, t, m) - \Delta \bar{x}^{\xi\kappa}(i_1 k_1)) \cdot (\Delta x^{\xi\eta\kappa}(i_2 j k_2, t, m) - \Delta \bar{x}^{\xi\kappa}(i_2 k_2)), \quad (7)$$

where $\hat{\sigma}^{\xi\kappa}(ik)$ and $\Delta \bar{x}^{\xi\kappa}(ik)$ are given in (4) and (5). Similarly, an entry of \mathbf{FFc}^{η} between grids j_1 and j_2 in the alongshore direction is

$$C^{\eta}(j_1, j_2) = \frac{1}{\hat{\sigma}^{\eta}(j_1) \hat{\sigma}^{\eta}(j_2)} \frac{1}{N^{\xi} N^{\kappa} M_t M_{en}} \sum_{i=1}^{N^{\xi}} \sum_{j=1}^{N^{\kappa}} \sum_{t=1}^{M_t} \sum_{m=1}^{M_{en}} \cdot (\Delta x^{\xi\eta\kappa}(ij_1 k, t, m) - \Delta \bar{x}^{\eta}(j_1)) \cdot (\Delta x^{\xi\eta\kappa}(ij_2 k, t, m) - \Delta \bar{x}^{\eta}(j_2)) \quad (8)$$

where

$$(\hat{\sigma}^{\eta}(j))^2 = \frac{1}{N^{\xi} N^{\kappa} M_t M_{en}} \sum_{i=1}^{N^{\xi}} \sum_{j=1}^{N^{\kappa}} \sum_{t=1}^{M_t} \sum_{m=1}^{M_{en}} \cdot (\Delta x^{\xi\eta\kappa}(ijk, t, m) - \Delta \bar{x}^{\eta}(j))^2 \quad (9)$$

$$\Delta \bar{x}^{\eta}(j) = \frac{1}{N^{\xi} N^{\kappa} M_t M_{en}} \sum_{i=1}^{N^{\xi}} \sum_{j=1}^{N^{\kappa}} \sum_{t=1}^{M_t} \sum_{m=1}^{M_{en}} \Delta x^{\xi\eta\kappa}(ijk, t, m). \quad (10)$$

[37] If the surrogate data set has a large enough sample, then the resulting correlations are locally smooth between neighboring grid points. However, spurious correlations can occur between remote grid points, leading to undesirably long tails in $\mathbf{FFc}^{\xi\kappa}$ and \mathbf{FFc}^{η} [Gaspari and Cohn, 1999]. Such long tails can cause noisy analysis increments. A common technique to address this problem is to apply a localization function that retains correlations computed from the surrogate data within a local neighborhood but suppresses all correlations at large distances. For localization of $\mathbf{FFc}^{\xi\kappa}$ and \mathbf{FFc}^{η} , we use a Gaussian matrix. The final correlation matrix is then given by the Hadamard (or Schur) product of a correlation matrix computed from the surrogate data and the Gaussian matrix.

[38] When using the Hadamard product to construct a correlation matrix, caution should be exercised: The Hadamard product produces a positive definite matrix only if both matrices are positive definite [e.g., Horn and Johnson, 1994]. While the correlation matrix estimated from the surrogate data is generally positive definite, the Gaussian matrix is not necessarily so, especially for large length scales. In ROMS3DVAR a Cholesky factorization is applied to the correlation matrices for preconditioning [Li *et al.*, 2008, section 4.1]. The use of the LAPACK code for the

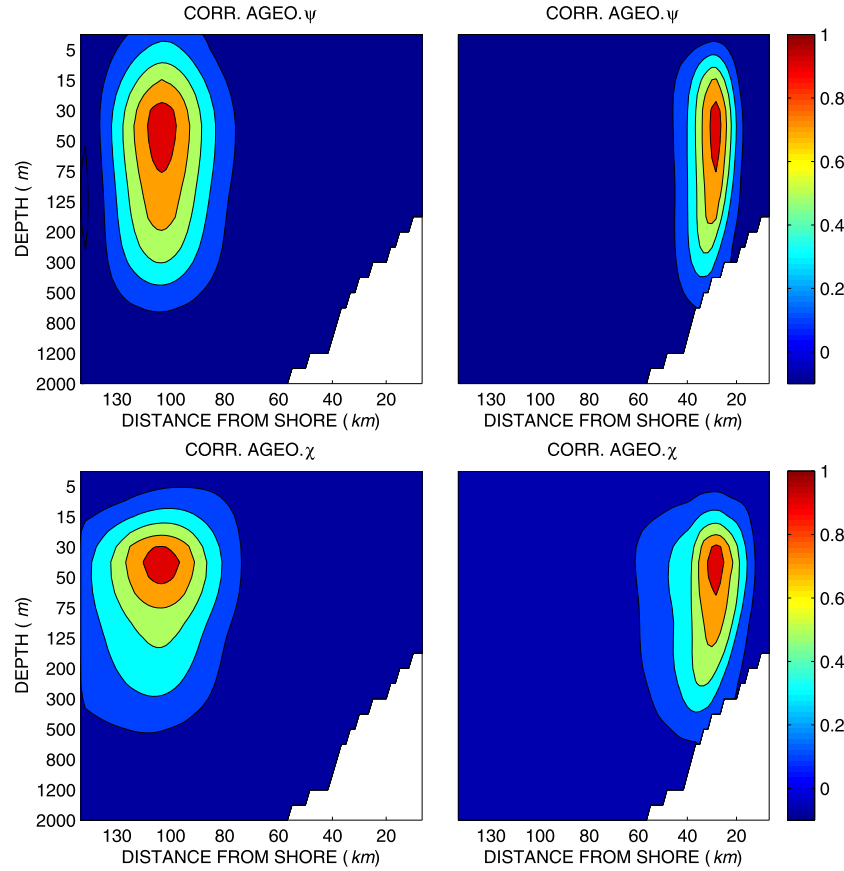


Figure 7. Vertical cross-shore correlation of ageostrophic streamfunction $C_{\psi''\psi''}^{\xi\kappa}(i_1k_1, i_2k_2)$ (top) and ageostrophic velocity potential $C_{\chi''\chi''}^{\xi\kappa}(i_1k_1, i_2k_2)$ (bottom) for fixed (i_1k_1) at (left) an offshore location and (right) a nearshore location and varying (i_2k_2) in the vertical cross-shore section. The depth of (i_1k_1) is 50 m.

Cholesky factorization acts as a verification of the positive definiteness of $\mathbf{FFc}^{\xi\kappa}$ and \mathbf{FFc}^η [Anderson et al., 1999].

3.3.2. Application

[39] For the localization of $\mathbf{FFc}^{\xi\kappa}$ and \mathbf{FFc}^η in ROMS3D-VAR, we use a Gaussian matrix with a horizontal length scale of 50 km and a vertical length scale of 400m. For the nonsteric SSH, the 2-D correlation $C_{\zeta'\zeta'}^\eta(i_1j_1, i_2j_2)$ is described by Li et al. [2008]. The decorrelation length scale of $\mathbf{FFc}_{\zeta'\zeta'}^{\xi\kappa}$ is about 10 km nearshore, increases to about 35 km further offshore and remains the same beyond 80 km offshore. Here the decorrelation length scale is estimated as the distance to the point where the correlation reduces to e^{-1} . In contrast, $\mathbf{FFc}_{\zeta'\zeta'}^\eta$ is basically homogeneous with the decorrelation length of about 30km, although the decorrelation length scale decreases slightly around the latitude of Monterey Bay.

[40] Figure 7 shows the 2-D correlations $C^{\xi\kappa}(i_1k_1, i_2k_2)$ of ageostrophic streamfunction $\mathbf{FFc}_{\psi''\psi''}^{\xi\kappa}$ and ageostrophic velocity potential $\mathbf{FFc}_{\chi''\chi''}^{\xi\kappa}$, for fixed (i_1k_1) at either an offshore or a nearshore location and varying (i_2k_2) in the vertical cross-shore section. The property of the 1-D alongshore correlations $\mathbf{FFc}_{\psi''\psi''}^\eta$ and $\mathbf{FFc}_{\chi''\chi''}^\eta$ are similar to those of $\mathbf{FFc}_{\zeta'\zeta'}^\eta$, that is, they are basically homogeneous with the decorrelation length of about 30 km.

[41] A slight difference between $\mathbf{FFc}_{\psi''\psi''}^{\xi\kappa}$ and $\mathbf{FFc}_{\chi''\chi''}^{\xi\kappa}$ appears in Figure 7 in the decorrelation length scale:

$\mathbf{FFc}_{\psi''\psi''}^{\xi\kappa}$ has slightly larger vertical but smaller cross-shore decorrelation length scale than $\mathbf{FFc}_{\chi''\chi''}^{\xi\kappa}$. Otherwise $\mathbf{FFc}_{\psi''\psi''}^{\xi\kappa}$ and $\mathbf{FFc}_{\chi''\chi''}^{\xi\kappa}$ have quite similar spatial patterns. In general, the cross-shore decorrelation length scale decreases as the distance from the coast increases, while the vertical decorrelation length scale does not change in the cross-shore direction.

[42] Figure 8 shows the 2-D correlation $C^{\xi\kappa}(i_1k_1, i_2k_2)$ of temperature $\mathbf{FFc}_{TT}^{\xi\kappa}$ for (i_1k_1) fixed at offshore and nearshore locations at depths of 50 m and 200 m. The behavior of $\mathbf{FFc}_{TT}^{\xi\kappa}$ is quite similar to that of $\mathbf{FFc}_{\psi''\psi''}^{\xi\kappa}$ and $\mathbf{FFc}_{\chi''\chi''}^{\xi\kappa}$, but the decorrelation length scales of $\mathbf{FFc}_{TT}^{\xi\kappa}$ are slightly larger in the cross-shore direction and smaller in the vertical direction than those of $\mathbf{FFc}_{\psi''\psi''}^{\xi\kappa}$ and $\mathbf{FFc}_{\chi''\chi''}^{\xi\kappa}$. Moreover, the cross-shore variation of the vertical decorrelation length scale is fairly small. Variations in the decorrelation length scale, smaller near the surface, can be explained by the dominance of baroclinic normal modes. The properties of the 1-D alongshore correlation \mathbf{FFc}_{TT}^η are similar to those of $\mathbf{FFc}_{\zeta'\zeta'}^\eta$, as well as those of $\mathbf{FFc}_{\psi''\psi''}^\eta$ and $\mathbf{FFc}_{\chi''\chi''}^\eta$.

[43] The vertical cross-shore correlation of salinity $C_{SS}^{\xi\kappa}(i_1k_1, i_2k_2)$ is shown in Figure 9. While decorrelation length scales are very similar to those of $\mathbf{FFc}_{TT}^{\xi\kappa}(i_1k_1, i_2k_2)$, the slant structure of $C_{SS}^{\xi\kappa}(i_1k_1, i_2k_2)$ nearshore suggests a strong influence of the thermocline variability as observed in $\Sigma_{SS}^{\xi\kappa}$ (Figure 6). The larger vertical decorrelation length

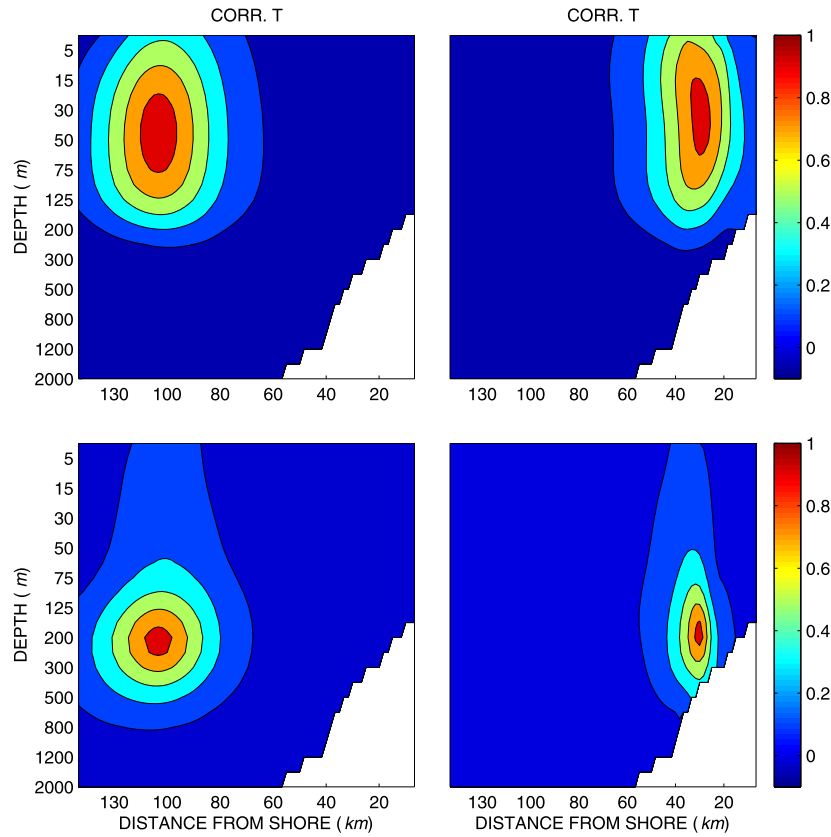


Figure 8. Vertical cross-shore correlation of temperature $C_{TT}^{\xi\kappa}(i_1 k_1, i_2 k_2)$ for fixed $(i_1 k_1)$ at an (left) offshore and (right) nearshore location at (top) a depth of 50 m and (bottom) at a depth of 200 m and varying $(i_2 k_2)$.

scales nearshore for salinity are understandable. They reflect the fact that, during upwelling, salinity near the surface is controlled by the amount of upwelled deep water. This feature contributes to the significance of the inseparability in the cross-shore and vertical directions. The properties of the 1-D alongshore correlation \mathbf{FFc}_{SS}^{η} are similar to those of $\mathbf{FFc}_{\zeta\zeta}^{\eta}$ and \mathbf{FFc}_{TT}^{η} .

[44] From Figures 8 and 9, we can see the variation of the vertical decorrelation length scale with depth. The vertical decorrelation length scale becomes larger with depth. This variation is also similar for the ageostrophic streamfunction and velocity potential, though their vertical decorrelation length scales are larger overall than those of temperature and salinity.

[45] In ROMS3DVAR, the cross-correlation $\mathbf{FFc}_{TS}^{\xi\kappa}$ between temperature and salinity is parameterized by the local cross-correlation vector \mathbf{FFr}_{TS} and the average of the corresponding self-correlations $\mathbf{FFc}_{TT}^{\xi\kappa}$ and $\mathbf{FFc}_{SS}^{\xi\kappa}$ [Li et al., 2008, equation (24)]. Figure 10 shows \mathbf{FFr}_{TS} at the surface and at a depth of 75 m.

4. Single-Observation Experiments

[46] Experiments using a single observation are simple yet they can yield insight into how a data assimilation system works [Parrish and Derber, 1992; Thepaut et al., 1996]. They demonstrate the function of the background error covariance matrices, the role of the constraints, and the sensitivity of the system to the type and location of

observations. They also illustrate how observed information propagates vertically, which is an intricate task for any ocean data assimilation system because of the extremely sparse observations in the deep ocean and the presence of the mixed layer and thermocline. In ROMS3DVAR, this task is undertaken by the hydrostatic balance and vertical error correlations. In addition, single observation experiments are quite effective in verifying the computer code.

4.1. SSH Observation

[47] SSHs are observed with satellite altimetry and tide gauges. SSH observations have been a major data source for ocean data assimilation owing to, not only wide availability, but also their ability to constrain the temperature and salinity profiles through the hydrostatic balance [e.g., Cooper and Haines, 1996]. A weak hydrostatic balance constraint is essential for coastal data assimilation. As shown in Figure 3 for the standard deviation, the nonsteric SSH dominates steric SSH near the coast. This suggests that the use of a strong constraint is unreasonable there. In contrast, the steric SSH dominates in the offshore region. This implies that without the weak or strong constraint, the background error covariance matrix must include the cross-correlations between total SSH, temperature, and salinity. These cross-correlations are inhomogeneous and have long vertical decorrelation length scales. It is difficult to reconcile such complex relations in the cross-correlations in a way that is computationally feasible for an incremental 3DVAR algorithm.

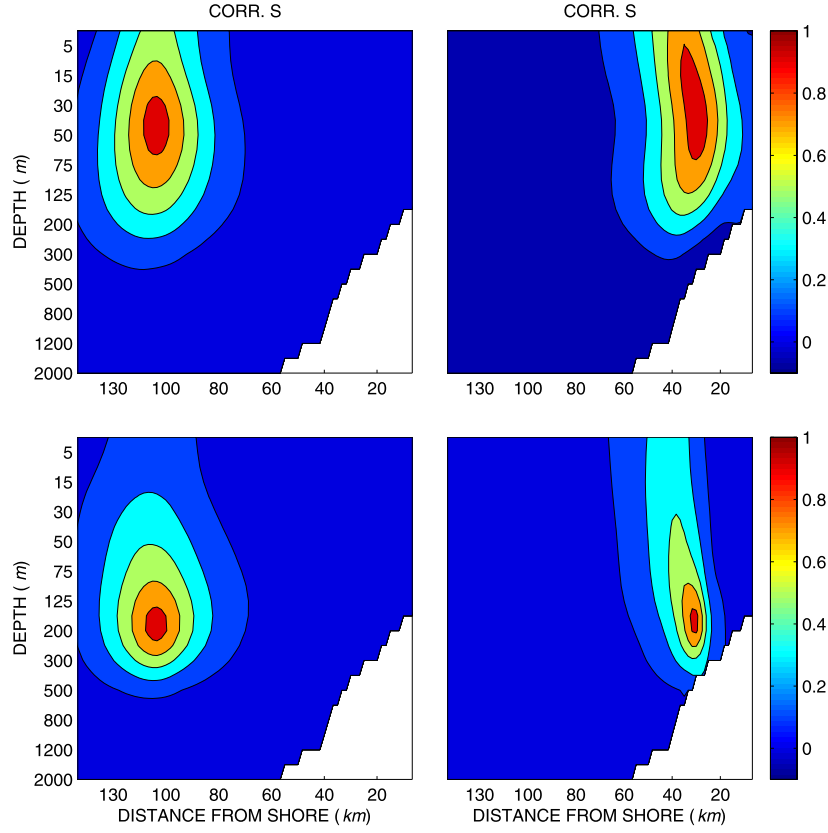


Figure 9. Same as Figure 6 but for salinity $C_{SS}^{\xi\kappa}(i_1k_1, i_2k_2)$.

[48] In the absence of other types of observations, a SSH observation induces analysis increments in the three ROMS3DVAR control variables, $\delta\mathbf{FF}x_{C_s}^a$, $\delta\mathbf{FF}x_{T_s}^a$, and $\delta\mathbf{FF}x_{S_s}^a$, by invoking the weak constraint for hydrostatic balance. Geostrophic balance is, however, applied as a strong constraint. Thus, the velocity increment is strictly determined by $\delta\mathbf{FF}x_{C_s}^a$, $\delta\mathbf{FF}x_{T_s}^a$, and $\delta\mathbf{FF}x_{S_s}^a$.

[49] Figure 11 shows the analysis increment using a single SSH observation at an offshore location with a positive innovation, i.e., the value of the observation is higher than that of the ROMS3DVAR forecast. Both steric and nonsteric SSH increments are positive, leading to

geostrophic velocity increments that have an anticyclonic eddy-like structure. The positive steric SSH increment is related to a positive temperature increment and a negative salinity increment. An anisotropic effect of the decorrelation length scale in the error correlations is visible in the length scales of the increments that are larger in the alongshore direction. If the observation were taken exactly at a ROMS3DVAR grid point, then the nonsteric SSH increment would have a similar spatial pattern to the horizontal error correlation $\mathbf{FF}c^{\xi\eta} = \mathbf{FF}c^{\xi} \otimes \mathbf{FF}c^{\eta}$ that assumes horizontal separability [Li *et al.*, 2008, Figure 3]. Therefore, an observation function can act as a smoother when the

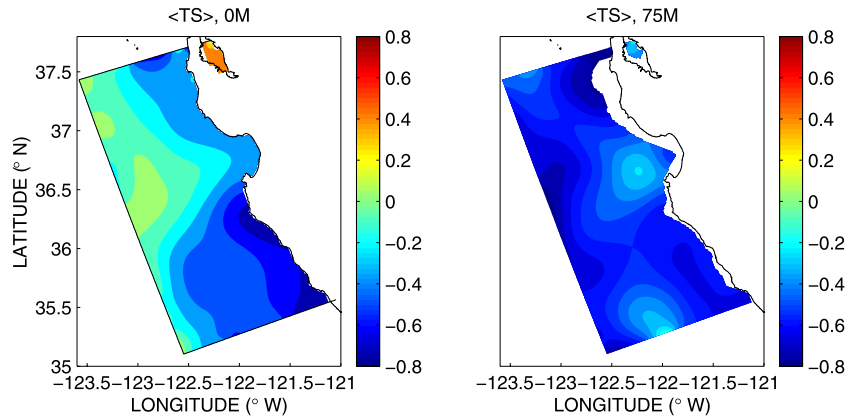


Figure 10. Local cross-correlation \mathbf{Fr}_{TS} between the temperature and salinity (left) at the surface and (right) at a depth of 75 m.

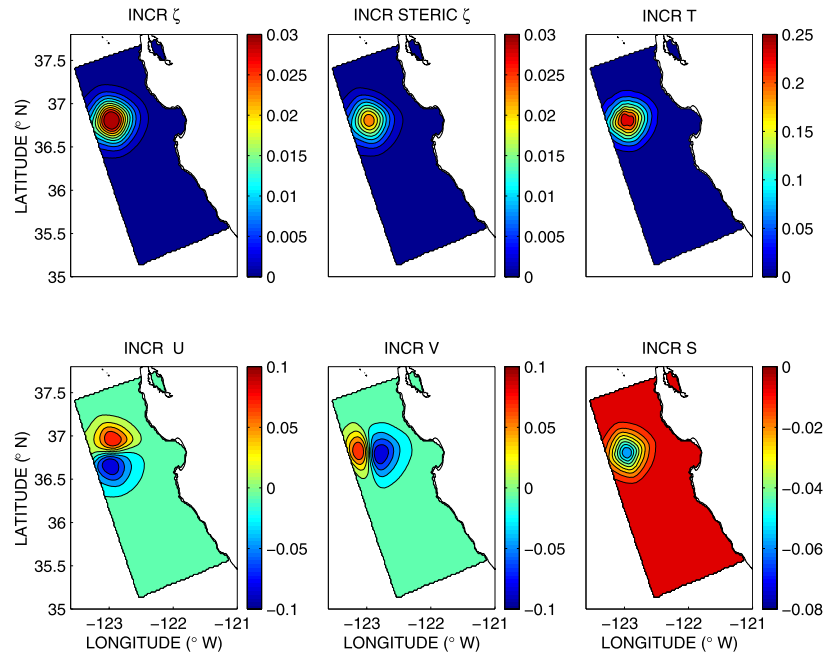


Figure 11. Analysis increments for total SSH, steric SSH, temperature, salinity, and geostrophic velocity components at the sea surface using a SSH observation at an offshore location, 123.0°W and 36.8°N. The unit is meters for SSH, °C for temperature, psu for salinity, and meters per second for velocity. The innovation is 0.048 m, i.e., the observed value is higher than the ROMS forecast. The standard deviation of the observation error is 0.025 m.

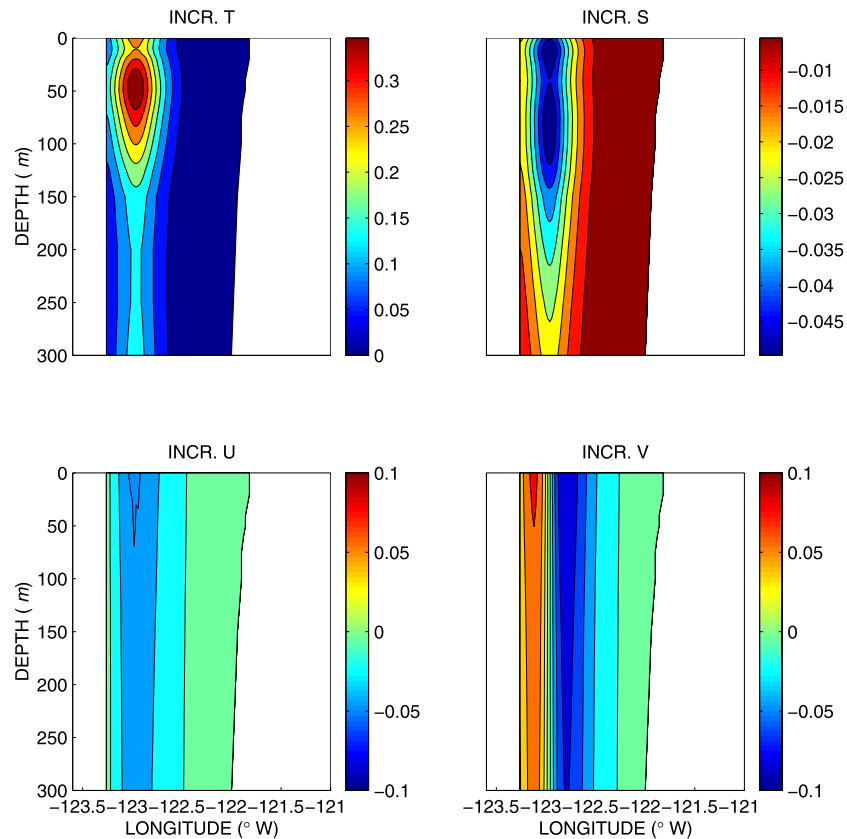


Figure 12. Analysis increments in the vertical section at 36.8°N corresponding to Figure 11.

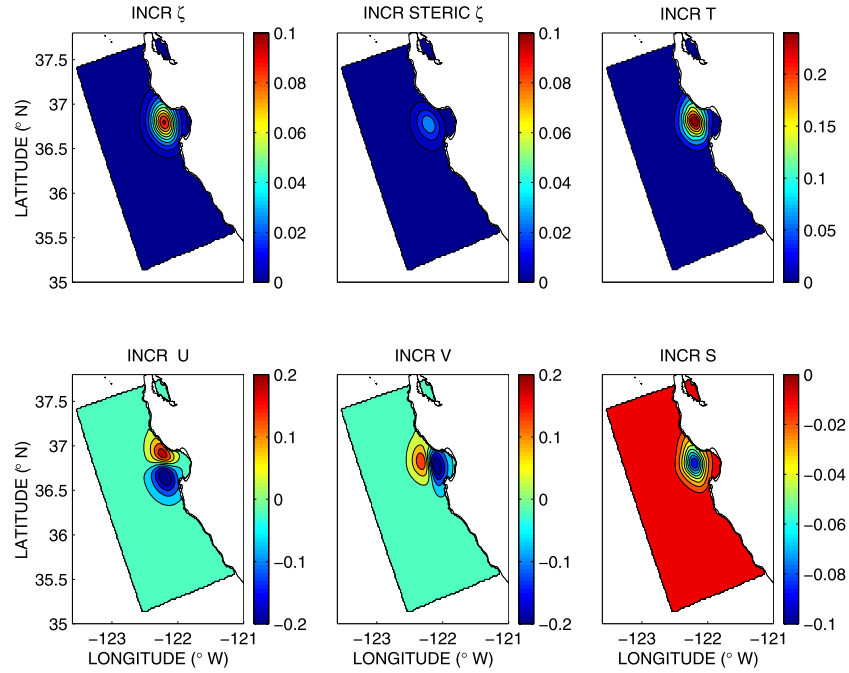


Figure 13. Analysis increments using a SSH observation at a location, 122.2°W and 36.8°N nearshore. The innovation is 0.115 m. Others are the same as Figure 11.

corresponding observation is not taken at a ROMS3DVAR grid point.

[50] The vertical spread of the observed information is shown in Figure 12 for the same experiment. The increments are mainly contained above a depth of 150 m. The maxima of the temperature and salinity increments are centered at about 50 m, which is around the bottom of the mixed layer. Both geostrophic velocity increments have their maximum at the surface but penetrate deeper than the temperature and salinity increments. This is due to the barotropic pressure gradient induced by the nonsteric SSH increments.

[51] To examine the sensitivity to observation location, we carry out another experiment with a single nearshore observation. The analysis increments are shown in Figure 13. All increments have smaller length scales than in the offshore experiments due to the cross-shore inhomogeneity of the decorrelation length scales (section 3.3.2).

[52] The steric SSH increment is much less dominant in comparison with the offshore observation. The steric SSH increment accounts for more than 80% of the total SSH increment in the offshore case, while it accounts for only about 30% in the nearshore case. The non-steric SSH increment is more important than the steric SSH increment nearshore, which is consistent with the ratio of the nonsteric and steric error variances as can be inferred from Figure 3.

4.2. Along-Shore Velocity Observation

[53] In the absence of other types of observations, a velocity observation induces analysis increments in the four ROMS3DVAR control variables, δFFx_{η}^a , δFFx_{χ}^a , δFFx_T^a , and δFFx_S^a , through the weak constraint for the geostrophic balance. Total velocity increments have both geostrophic and ageostrophic components and hence depend on all four control variables. The relative amplitude of the geostrophic and ageostrophic increments depends on the relative ampli-

tude of the corresponding standard deviations: in general, ageostrophy is significant near the coast while geostrophy rules in the offshore region. The SSH increment is completely determined by δFFx_T^a and δFFx_S^a because hydrostatic balance is applied as a strong constraint.

[54] Figure 14 shows the analysis increment using a single observation of alongshore velocity at a nearshore location with a positive innovation. The increment of the total cross-shore velocity shows a classic “butterfly-like” structure. One interesting result is the relative value of the geostrophic velocity and ageostrophic velocity. The geostrophic velocity accounts for about 60% of the total.

4.3. Temperature Observation

[55] Temperature is the most observed variable in the ocean. In the absence of other types of observations, a temperature observation induces analysis increments in two control variables, δFFx_T^a and δFFx_S^a ; the latter is caused by the cross-correlation $FFc_{TS}^{\eta\kappa}$ between them. Both hydrostatic balance and geostrophic balance are applied as strong constraints; hence δFFx_T^a and δFFx_S^a completely determine the SSH and velocity increments.

[56] Figure 15 shows the analysis increment for a single observation of temperature at a nearshore location with a positive innovation. The increment structures of the velocity components are classic ones. The increment of salinity is obviously due to the cross-correlation. Consistent with Figure 10, the cross-correlation is negative nearshore, and thus the increments of salinity and temperature are opposite in sign.

5. Application to the AOSN Experiment

[57] This section demonstrates the performance of ROMS3DVAR using observations from the AOSN field

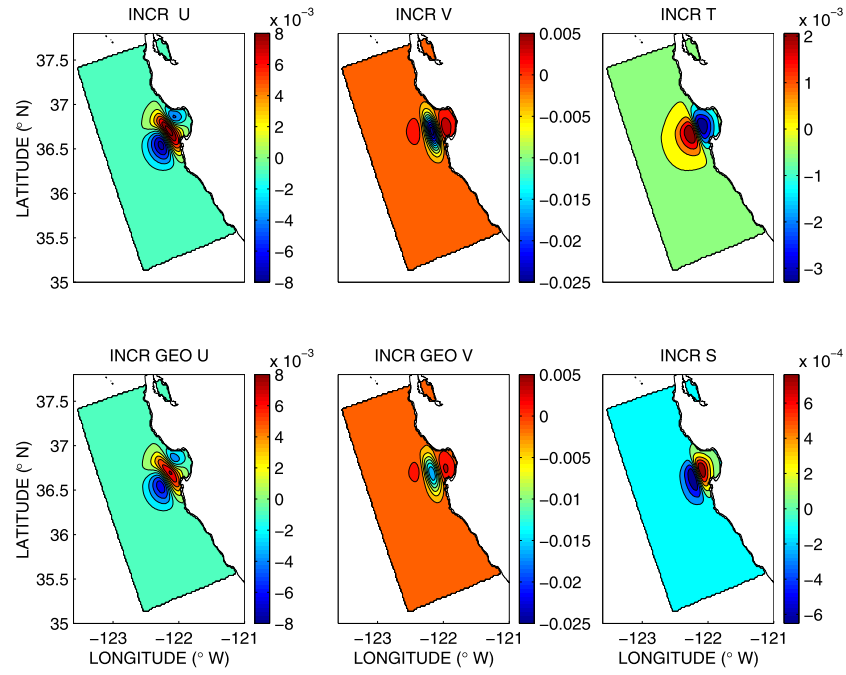


Figure 14. Analysis increments for total velocity components, geostrophic velocity components, temperature and salinity at the sea surface using a single observation of the alongshore velocity at a nearshore location, 122.2°W and 36.8°N. The innovation is -0.03 m/s. The standard deviation of the observation error variance is 0.1 m/s. The units are °C for temperature, psu for salinity, and meters per second for velocity.

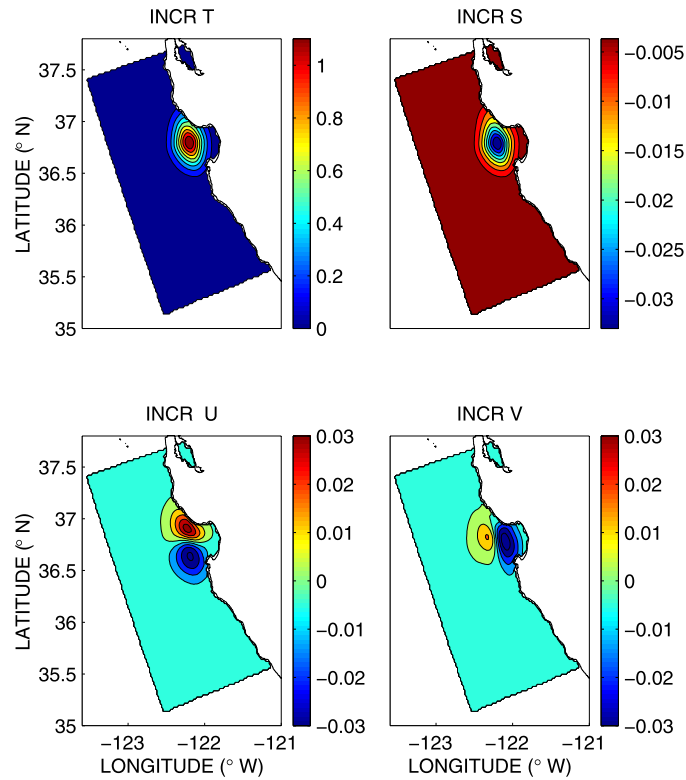


Figure 15. Analysis increments for temperature, salinity, and geostrophic velocity components at the sea surface using a single offshore temperature observation at a nearshore location at 122.2°W and 36.8°N. The innovation is 1.3°C . The standard deviation of the observation error is 0.35°C . The units are °C for temperature, psu for salinity, and meters per second for velocity.

experiment in August 2003. ROMS3DVAR was executed in real-time during the AOSN experiment, but the results presented here are from the postexperiment analysis, which we call reanalysis. After describing the AOSN experiment, we mainly focus on two aspects. For demonstration of the robustness, we present results from a rapid flow transition from upwelling to relaxation forced by a change in atmospheric wind stress. For an objective evaluation of the ROMS3DVAR, we compare the results with two sets of independent observations that have not been assimilated. A more detailed description of the reanalysis results can be found in the work of Chao et al. (submitted manuscript, 2008).

5.1. AOSN and ROMS3DVAR

[58] The AOSN experiment in Monterey Bay, California, August 2003, provided an unprecedented number of in situ observations by a variety of means and instruments; details of the experiment can be found at the Web site (<http://www.mbari.org/aosn>). During August 2003, ROMS3DVAR generated analyses and forecasts in real-time using the 6-h forecast cycle (section 2.2). After the experiment, additional observations became available while some of the original observations were upgraded. The results presented in this section are obtained using all observations available. The observations include the NAVOCEANO MCSST Level 2 High Resolution Picture Transmission and Local Area Coverage (HRPT/LAC) 2.2 km sea surface temperature data set (level 2), underwater glider temperature/salinity profiles, aircraft SSTs, ship temperature/salinity/depth (CTD), and Automatic Underwater Vehicle (AUV) temperature/salinity profiles (<http://www.mbari.org/aosn> for details about observations).

[59] In this reanalysis experiment we adjusted the weak geostrophic balance constraint. The geostrophic velocity is computed after smoothing is applied to δFFx_C , δFFx_T , and δFFx_S . The smoothing is a spatial average with the weight determined by the Gaussian function e^{-d^2/r_0^2} , where d is the distance and $r_0 = 3$ km (approximately two times the model grid size). This additional smoothing is used to reduce an overestimation of the geostrophic velocity at small scales due to the small decorrelation length scales nearshore. Also, it is a practical consideration. It has been shown that a minimization process generally acts first on the larger scales. Thus, the small scales are dealt with mainly during the last stage of the minimization process [Veerse and Thepaut, 1998]. In this experiment, we allow a maximum of 40 iterations for the minimization. In this case, it is possible that the minimization is terminated before it converges to the minimum of the cost function. In this case, some small-scale noise may remain. The smoothing can help reduce such small-scale noise.

5.2. Transition Between Upwelling and Relaxation

5.2.1. Synoptic Analysis

[60] The ocean responds quickly to changes in the atmosphere. In this region, atmospheric conditions are subject to strong diurnal variations as well as rapid weather changes. The ocean is particularly responsive to wind direction changes. Equatorward wind stress favors the upwelling of the cold water along the coastline, while poleward wind

stress causes relaxation, leading to warm surface and subsurface water. In August 2003, there were two major upwelling events (Figure 2). The first started on 6 August and was followed by relaxation from 20 to 22 August. The second upwelling event started on 23 August and ended by 30 August.

[61] The transition from the first upwelling state to the relaxation is shown in Figure 16 via the sea surface velocity and temperature for 18 to 21 August 2003. Nearshore there is a cold belt with temperatures as low as 10 to 12°C on 18 August. The surface currents are systematically equatorward near the coast. During the relaxation event the SST increases, and the cold upwelling centers both north and south of Monterey Bay are replaced by warm water by 21 August 2003. The SST increases are larger than 5°C in some locations.

[62] In association with the transition, the surface current also underwent a significant change. During the upwelling there is a systematic equatorward velocity jet, which follows closely the relatively large SST gradient zone nearshore. This jet is interrupted during the transition. The most significant change occurred within Monterey Bay, where the velocity reverses direction from equatorward to poleward. This direction reversal is well captured by ROMS3DVAR as seen in the comparison with the HF radar measurements presented next.

5.2.2. Comparison With HF Radar Observations

[63] A comparison with HF-radar velocity observations is ambitious for the present ROMS3DVAR because no velocity observations were assimilated. Therefore, the velocity analysis increment is strictly the result of a geostrophic balance [Li et al., 2008, section 4]. In contrast, the HF radar covers mainly Monterey Bay where ageostrophic velocities are significant. Moreover, the tidal velocities in this region can be as large as 0.1–0.2 m/s [Petruncio et al., 1998], which is comparable to the velocities arising from dynamic processes. ROMS does not include tidal forcing yet.

[64] For comparison purposes, we suppress the tidal signal in the HF radar observations by taking the average over 12 and 19 August 2003 for the first upwelling event and over 20 to 22 August 2003 for the relaxation event. The average also reduces the HF radar observational error. The observational error is generally considered to be 5–10 cm/s, but an averaged field should have much smaller errors. The corresponding composite maps are made from the ROMS3DVAR reanalysis. The results are shown in Figure 17.

[65] During the upwelling period, the HF radar observations show a jet-like structure that swerves in and out of the bay with a high speed. It also shows a cyclonic circulation within the bay. During the relaxation period the flow pattern changes drastically. The HF radar shows a cyclonic circulation dominating the entire bay. Differences from the upwelling flow pattern are most striking near the head of the Monterey Peninsula where the flow direction is reversed. These features in the upwelling and relaxation events are captured fairly well in the ROMS3DVAR reanalysis.

[66] To quantify the agreement of ROMS3DVAR with these observations, we use the correlation of the flow

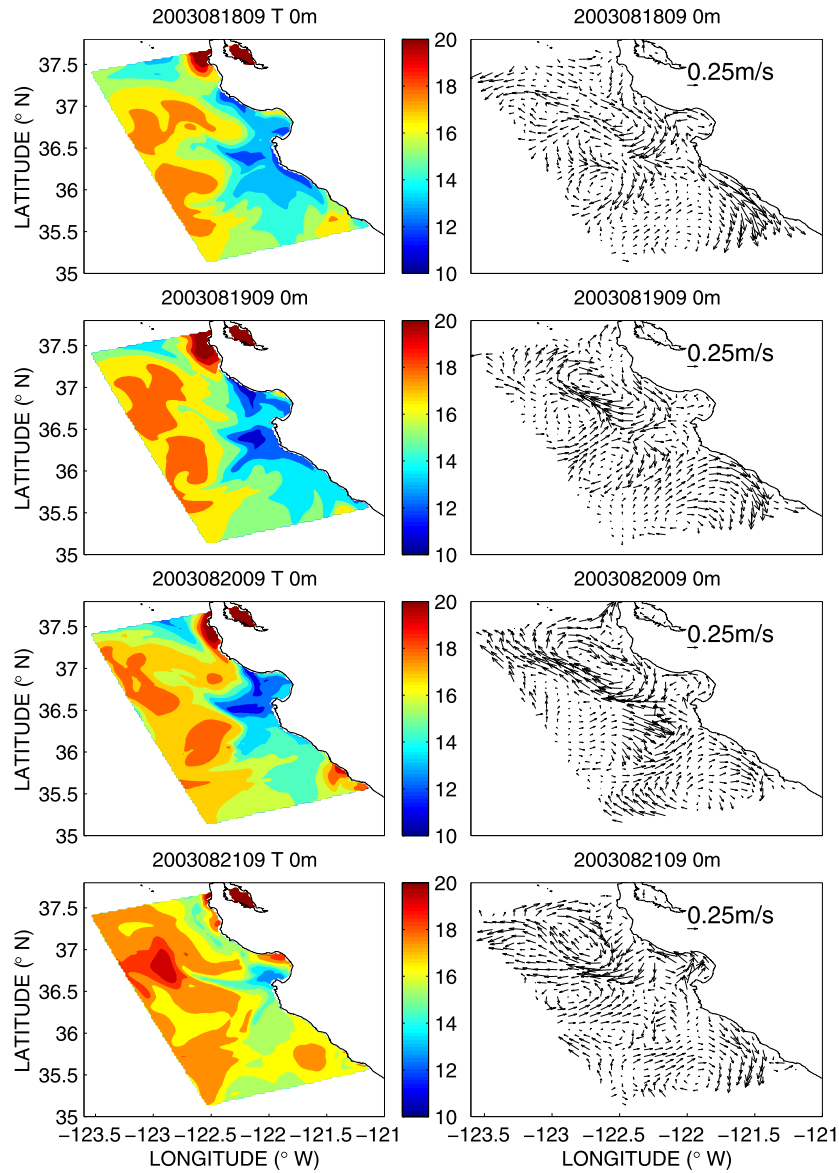


Figure 16. Temporal evolution of (left) sea surface temperature and (right) velocity in the ROMS3DVAR reanalysis during the transition period from upwelling (18 to 19 August 2003) to relaxation (20 to 21 August 2003).

patterns observed by the HF radar and the ROMS3DVAR reanalysis. The correlation is defined by

[67] Here a natural question is how much the data assimilation improves the representation of the sea surface

$$corr = \frac{\sum_{m=1}^{M^{HF}} [(u_m^{HF} - \bar{u}^{HF})(u_m^a - \bar{u}^a) + (v_m^{HF} - \bar{v}^{HF})(v_m^a - \bar{v}^a)]}{\sqrt{\sum_{m=1}^{M^{HF}} [(u_m^{HF} - \bar{u}^{HF})^2 + (v_m^{HF} - \bar{v}^{HF})^2]} \sqrt{\sum_{m=1}^{M^{HF}} [(u_m^a - \bar{u}^a)^2 + (v_m^a - \bar{v}^a)^2]}} \quad (11)$$

M^{HF} is the number of the HF radar observation for the corresponding event, the superscript HF stands for the HF radar, and $\{\cdot\}$ for the average over M^{HF} observation. The correlation is 0.82 for the upwelling period and 0.77 for the relaxation period. Overall, ROMS3DVAR has the capability to reproduce major features of the velocity field during this particular transition.

current described above. To answer this question, a simulation experiment is performed, starting from 1 August 2003. The model configuration is the same as the one used for the data assimilation experiment. The results are shown in the third row of Figure 17. The simulation produces a realistic southward jet-like current during the upwelling event as shown by the spatial correlation of 0.83 with the

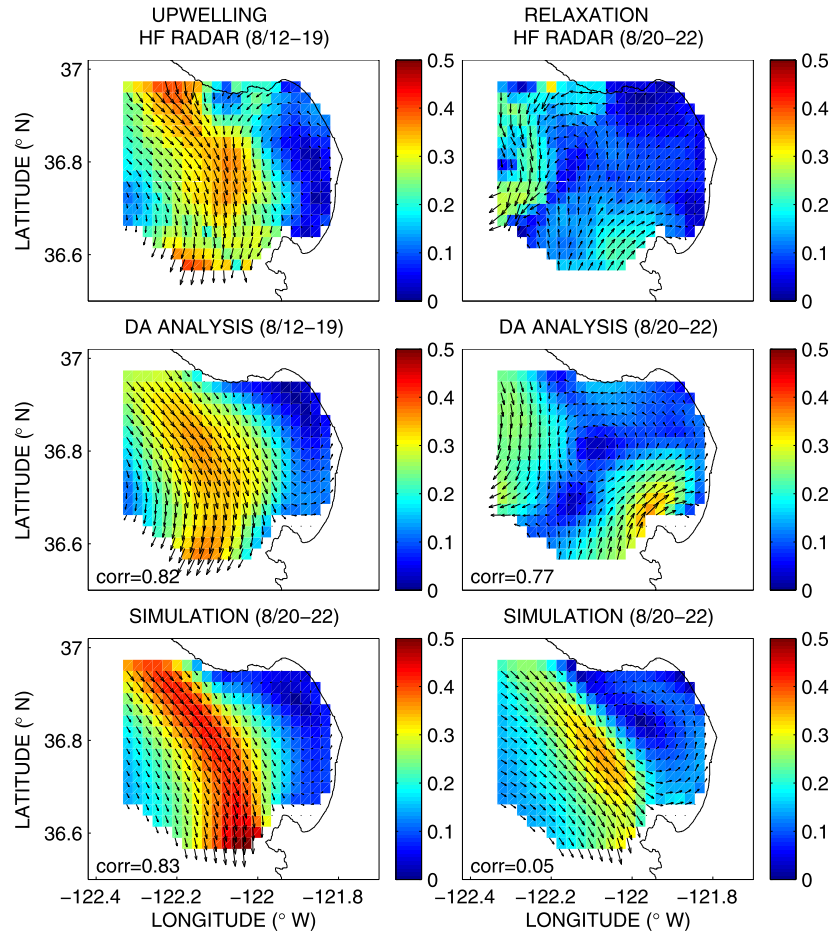


Figure 17. Comparison of (top) the averaged HF radar surface velocity and (middle) the ROMS3DVAR reanalysis during (right) the upwelling event between 12 and 19 August 2003 and (left) the relaxation event between 20 and 22 August 2003. (bottom) The corresponding currents from a simulation without data assimilation are also shown. The color represents the speed, and the unit is meters per second.

HF radar surface currents, but its velocity is overpredicted and the strong flow intrudes into the bay slightly too far. As a consequence, the current direction did not reverse within the bay during the relaxation. In contrast, in the reanalysis the upwelling front is well constrained, and thus the velocity and location of the jet-like current and the reversal of the current direction is realistically reproduced.

5.3. Evaluation With T/S Profiles at Mooring M2

[68] While a variety of evaluations were performed, we present here an evaluation of the ROMS3DVAR reanalysis using independent observations of T/S profiles at Mooring M2. The M2 mooring records profiles of T/S , velocities, and winds every 10 min. M2 is located near the boundary of warm offshore water and cold upwelled nearshore water (Figures 1 and 16). Hence, the ocean state at M2 is sensitive to the location of this boundary, which depends on the strength of upwelling. Because of the continuous nature of the measurements and their sensitivity to upwelling, we do not assimilate them but use them instead as an independent data set for evaluation.

[69] A comparison of the ROMS3DVAR reanalysis and the M2 observations is shown in Figure 18 for August 2003.

The M2 observations are averages over each 24-h time window, while the ROMS3DVAR data is the average of the four analyses produced each day.

[70] During the first upwelling event, the observed M2 temperatures became warmer near the surface, also more gradually below, until 20 August 2003 when the relaxation begins. This suggests that the M2 location was not affected by the upwelled cold water during this upwelling event. In fact, it was controlled by a warm tongue, which is the consequence of a complex “bifurcated-flow” structure of the cold water (Rosenfeld *et al.* [1994]; see 18 and 20 August in Figure 16). During the relaxation period, temperatures became cooler, rather than warmer as might have been expected. During the second upwelling event, temperatures rapidly became warmer. Overall, the observations suggest that warm temperatures are generally associated with lower salinity and cold temperatures with higher salinity. The ROMS3DVAR reanalysis shows a good agreement with these observed phenomena. The maximum root-mean squared error (RMSE) of the ROMS3DVAR reanalysis and the observation is centered around the bottom of the mixed layer at about 40 m for both temperature and salinity.

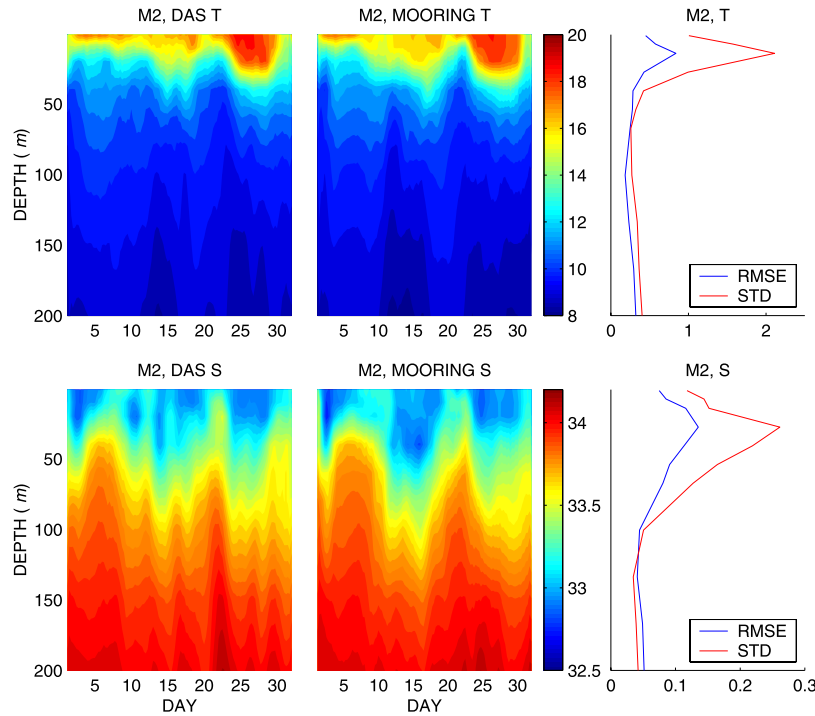


Figure 18. Comparison of the ROMS3DVAR reanalysis and M2 observations for August 2003: the temporal evolution (left two columns) of (top) temperature and (bottom) salinity for (left) the ROMS3DVAR reanalysis and (center) the M2 observations, and (right) the corresponding root-mean-square error (RMSE) and standard deviation (STD) of the M2 observations. Both the mooring and ROMS data are averaged over the time window of 24 h. Time is in days of August 2003. The unit is $^{\circ}\text{C}$ for temperature and psu for salinity.

The maximum RMSE is less than 1.0°C in temperature and 0.15 psu in salinity, in comparison with a maximum STD for the M2 observations of 2.3°C in temperature and 0.28 psu in salinity.

6. Summary and Discussions

[71] In the work of *Li et al.* [2008], we proposed a 3DVAR scheme for the coastal ocean. This scheme has the capability of incorporating inhomogeneous, anisotropic, and inseparable correlations and also weak geostrophic and hydrostatic balances. Here we demonstrated ways to take advantage of these capabilities and discussed their importance when the scheme is applied to the California coastal ocean, where inhomogeneity and anisotropy are significant.

[72] Concerning inhomogeneity, it was shown that the horizontal decorrelation length scale offshore can be as much as two times larger than that nearshore for the California coastal ocean. This is true for all the control variables. The decorrelation length scale turns out to be less than the Rossby radius of deformation nearshore, while it is larger than the Rossby radius offshore. One dynamic consequence of this inhomogeneity is that there are significant ageostrophic velocities nearshore. If the decorrelation length scales specified are too large, the ageostrophic velocity may be underestimated nearshore.

[73] The anisotropy was not significant offshore, but it was nearshore. For our case, the alongshore decorrelation

length scale can be as large as the alongshore dimension of the entire model domain nearshore (not shown). Dynamically this can be explained by the fact that the wind stress is systematically coherent in the region. However, such a large decorrelation length scale is not desirable in data assimilation [*Gaspari and Cohn*, 1999]. This complexity of the anisotropy requires a scheme to adjust to it. In ROMS3DVAR we conservatively used Schur production to limit the decorrelation length scale, and thus anisotropy was only partially taken into account.

[74] The standard deviation and correlation of the background error were estimated based on an ensemble of model simulations. A concern is that the method is an ad hoc one without solid theoretical and practical justification. One supportive argument is that the model forecast has larger errors in regions with larger variability. On the other hand, the inhomogeneity and anisotropy may be overestimated. We consider that the error variance structure and correlations obtained are only a preliminary estimate. They need to be improved upon when appropriate observations become available.

[75] ROMS3DVAR assimilated a variety of observational data collected during the AOSN experiment. These data included satellite and aircraft SSTs, ship CDT, T/S profiles from a fleet of gliders and AUVs. These observations came with differing degrees of accuracy and different time and space resolutions. All these observations were assimilated simultaneously, which demonstrated that ROMS3DVAR

has a strong capability of handling a large amount of observational data from different sources. On the other hand, ROMS3DVAR can assimilate any subset of the AOSN data. Actually, ROMS3DVAR was used for an Observational System Experiment (OSE) with the AOSN data. The OSE allowed users to assimilate any selected subset of the data. ROMS3DVAR worked reliably during AOSN, and also within the OSE framework. We attribute the reliability and robustness of the developed ROMS3DVAR to the particular 3-D error correlations and weak dynamic constraints used.

[76] The experiment with the AOSN observations further demonstrated the capability of the system to reproduce complex flow patterns during upwelling and relaxation, as well as the transition between the upwelling and relaxation regimes. It is especially encouraging that the results from ROMS3DVAR showed reasonable accuracy in comparison with independent observations from the M2 mooring and HF radar. Note that the mooring is located in the Monterey Submarine Canyon, while the HF radar measures the area over the Canyon head. These locations always present great challenges to coastal ocean modelers. The success of the data assimilation in these locations indicates that ROMS3DVAR has the capability of coping with complex bathymetry and dynamics.

[77] During the AOSN reanalysis, only temperature and salinity observations were assimilated, and the current was constrained through the weak geostrophic and hydrostatic balance. Since the velocity field during the transition between the upwelling and relaxation is reasonably reproduced, the weak geostrophic and hydrostatic balance formulation appears to work reasonably well.

[78] In this paper we presented the overall performance of ROMS3DVAR. Prediction skill is not addressed here, but extensive evaluations are presented in the work of Chao et al. (submitted manuscript, 2008). The sensitivity to and influence of individual data sets were not addressed. These are crucial and complicated issues, especially for sea surface height observations from satellite altimetry [Fu and Cazenave, 2000] and in situ tidal gauge and sea surface velocity observations from HF radar [Paduan and Grabe, 1997]. The particularly challenging difficulty in assimilation of SSH and velocity observations arises from the strong tides in coastal oceans. These issues will be addressed in subsequent papers.

[79] **Acknowledgments.** The research described in this publication was carried out, in part, at the Jet Propulsion Laboratory (JPL), California Institute of Technology, under a contract with the National Aeronautics and Space Administration (NASA). Computations were performed on an SGI Origin computer through the JPL Supercomputing Project. Support from the Office of Naval Research (ONR) under grants N00014-04-1-0166, N00014-04-1-0191, N00014-04-1-0401, and N00014-05-1-0293 is gratefully acknowledged. The discussion with J. Doyle and X. D. Hong at the Navy Research Laboratory is acknowledged. We appreciate P. Marchesiello, X. Capet, and A. Shchepetkin for setting up the nested ROMS configuration and for many stimulating discussions. We also thank J. Paduan at the Navy Postgraduate School and I. Shumann at the Navy Research Laboratory for discussions related to the HF radar.

References

- Akima, H. (1970), A new method of interpolation and smooth curve fitting based on local procedures, *J. Assoc. Comput. Mach.*, **4**, 589–602.
- Anderson, E., et al. (1999), *LAPACK Users' Guide*, 3rd ed., 407 pp., SIAM, Philadelphia, Pa.
- Arakawa, A., and V. R. Lamb (1977), Computational design of the basic dynamical processes of the UCLA general circulation model, in *Methods in Computational Physics*, vol. 17, edited by J. Chang, pp. 173–265, Academic, New York.
- Barker, D. M., W. Huang, Y. R. Guo, A. J. Bourgeois, and Q. N. Xiao (2004), A three-dimensional variational data assimilation system for MM5: Implementation and initial results, *Mon. Weather Rev.*, **132**, 897–914.
- Blayo, E., and L. Debreu (1999), Adaptive mesh refinement for finite-difference ocean models: First experiments, *J. Phys. Oceanogr.*, **29**, 1239–1250.
- Chao, Y., Z. Li, J. Kindle, F. Chavez, and J. Paduan (2003), A high-resolution surface vector wind product for coastal oceans: Blending satellite scatterometer measurements with regional mesoscale atmospheric model simulations, *Geophys. Res. Lett.*, **30**(11), 1013, doi:10.1029/2002GL015729.
- Cooper, M., and K. Haines (1996), Altimetric assimilation with water property conservation, *J. Geophys. Res.*, **101**, 1059–1077.
- Daley, R. (1991), *Atmospheric Data Assimilation*, Cambridge Atmos. and Space Sci. Ser., 457 pp., Cambridge Univ. Press, Cambridge, U. K.
- Fu, L.-L., and A. Cazenave (Eds.) (2000), *Satellite Altimetry and Earth Sciences: A Handbook of Techniques and Applications*, 463 pp., Academic, New York.
- Fukumori, I., R. Raghunath, and L.-L. Fu (1998), Nature of global large-scale sea level variability in relation of atmospheric forcing: A modeling study, *J. Geophys. Res.*, **103**, 5493–5512.
- Gaspari, G., and S. E. Cohn (1999), Construction of correlation functions in two and three dimensions, *Q. J. R. Meteorol. Soc.*, **125**, 723–757.
- Hickey, B. (1998), Coastal oceanography of Western North America from the tip of Baja California to Vancouver Island, *Sea*, **11**, 345–393.
- Hodur, R. M. (1997), The Naval Research Laboratory's Coupled Ocean/Atmosphere Mesoscale Prediction System (COAMPStm), *Mon. Weather Rev.*, **125**, 1414–1430.
- Hollingsworth, A., and P. Lonnberg (1986), The statistical structure of short-range forecast error as determined from radiosonde data. Part I: The wind fields, *Tellus, Ser. A*, **38**, 111–136.
- Horn, R. A., and C. R. Johnson (1994), *Topics in Matrix Analysis*, 615 pp., Cambridge Univ. Press, New York.
- Kondo, J. (1975), Air-sea bulk transfer coefficients in diabatic conditions, *Boundary Layer Meteorol.*, **9**, 91–112.
- Large, W. G., and S. Pond (1982), Sensible and latent heat flux measurements over the ocean, *J. Phys. Oceanogr.*, **12**, 464–482.
- Li, Z., Y. Chao, and J. C. McWilliams (2006), Computation of the streamfunction and velocity potential for limited and irregular domains, *Mon. Weather Rev.*, **134**, 3384–3394.
- Li, Z., Y. Chao, J. C. McWilliams, and K. Ide (2008), A three-dimensional variational data assimilation scheme for the Regional Ocean Modeling System, *J. Atmos. Oceanic Technol.*, in press.
- Marchesiello, P., J. C. McWilliams, and A. F. Shchepetkin (2001), Open boundary conditions for long-term integration of regional ocean models, *Ocean Modell.*, **3**, 1–20.
- Marchesiello, P., J. C. McWilliams, and A. F. Shchepetkin (2003), Equilibrium structure and dynamics of the California Current System, *J. Phys. Oceanogr.*, **33**, 753–783.
- Paduan, J. D., and H. C. Graber (1997), Introduction to high-frequency radar: Reality and myth, *Oceanography*, **10**, 36–39.
- Parrish, D. F., and J. C. Derber (1992), The National Meteorological Center's spectral-interpolation system, *Mon. Weather Rev.*, **120**, 1747–1763.
- Petruncio, E. T., L. K. Rosenfeld, and J. D. Paduan (1998), Observations of the internal tide in Monterey Canyon, *J. Phys. Oceanogr.*, **28**, 1873–1903.
- Phillips, N. A. (1986), The spatial statistics of random geostrophic modes and first-guess error, *Tellus, Ser. A*, **38**, 137–161.
- Rabier, F., A. McNally, E. Andersson, P. Courtier, P. Uden, J. Eyre, A. Hollingsworth, and F. Bouttier (1998), The ECMWF implementation of three-dimensional variational assimilation (3D-Var). II: Structure functions, *Q. J. R. Meteorol. Soc.*, **124**, 1809–1829.
- Rosenfeld, L. K., F. B. Schwing, N. Garfield, and D. C. Tracy (1994), Bifurcated flow from an upwelling center: A cold water source for Monterey Bay, *Cont. Shelf Res.*, **14**, 931–964.
- Shchepetkin, A. F., and J. C. McWilliams (2003), A method for computing horizontal pressure-gradient force in an ocean model with a non-aligned vertical coordinate, *J. Geophys. Res.*, **108**(C3), 3090, doi:10.1029/2001JC001047.
- Shchepetkin, A. F., and J. C. McWilliams (2005), The Regional Ocean Modeling System: A split-explicit, free-surface, topography-following-coordinate ocean model, *Ocean Modell.*, **9**, 347–404.

- Shchepetkin, A. F., and J. C. McWilliams (2008), Computational kernel algorithms for fine-scale, multi-process, long-time oceanic simulations, in *Handbook of Numerical Analysis Special Volume: Computational Methods for the Atmosphere and the Oceans*, edited by R. Temam and J. Tribbia, Elsevier, New York, in press.
- Song, Y. T., and D. B. Haidvogel (1994), A semi-implicit ocean circulation model using a generalized topography-following coordinate system, *J. Comput. Phys.*, *115*, 228–244.
- Thepaut, J.-N., P. Courtier, P. G. Belaud, and G. Lemaitre (1996), Dynamical structure functions in a four-dimensional variational assimilation: A case study, *Q. J. R. Meteorol. Soc.*, *122*, 535–561.
- Veerse, F., and J.-N. Thepaut (1998), Multiple-truncated incremental approach for four-dimensional variational assimilation, *Q. J. R. Meteorol. Soc.*, *124*, 1889–1908.
-
- Y. Chao and Z. Li, Jet Propulsion Laboratory, California Institute of Technology, 4800 Oak Grove Drive, Pasadena, CA 91109, USA. (zhijin.li@jpl.nasa.gov)
- K. Ide and J. C. McWilliams, Department of Atmospheric and Oceanic Sciences and Institute of Geophysics and Planetary Physics, University of California, Los Angeles, CA 90095-1565, USA.